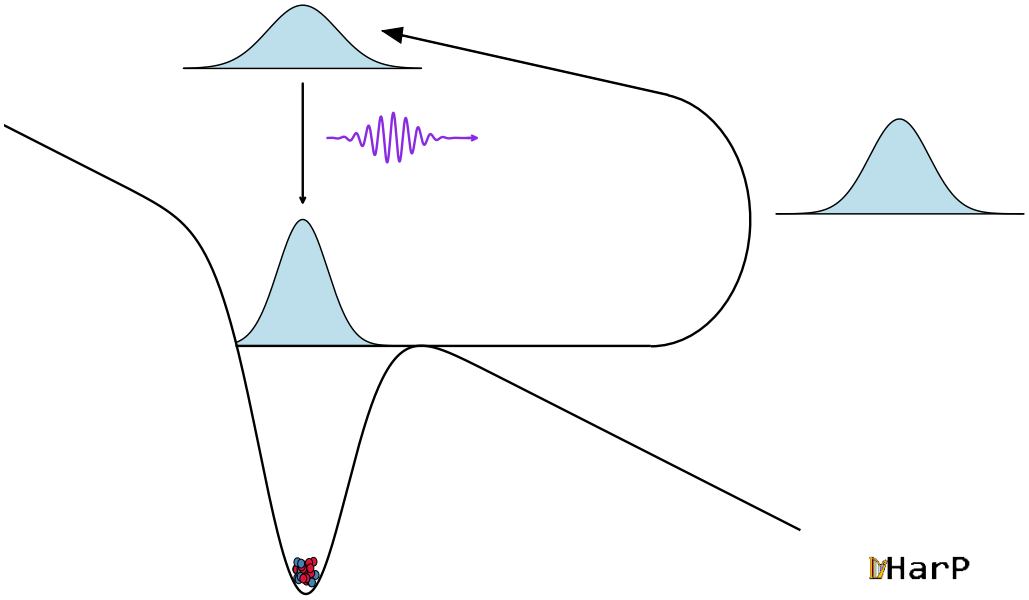

Numerical Modelling of High Harmonic Generation in Gases

Thesis for the degree of Master of Science in Physics

Linus Hagedorn

DEPARTMENT OF PHYSICS AND ASTRONOMY

Chalmers University of Technology

Gothenburg, Sweden 2026

www.chalmers.se

Master's thesis 2026

Numerical Modelling of High Harmonic Generation in Gases

Linus Hagedorn

CHALMERS

Department of Physics and Astronomy
Division of Subatomic, High Energy and Plasma Physics
Chalmers University of Technology
Gothenburg, Sweden 2026

Numerical Modelling of High Harmonic Generation in Gases
Linus Hagedorn

Supervisor: Dominika Maslárová, Division of Subatomic, High Energy and Plasma Physics
Examiner: Tünde Fülöp, Division of Subatomic, High Energy and Plasma Physics

Division of Subatomic, High Energy and Plasma Physics
Department of Physics and Astronomy
Chalmers University of Technology
SE-412 96 Gothenburg
Sweden
Telephone +46 (0)31-772 1000

Cover: Shows the three step model for high harmonic generation together with HarP's logo.
Typeset in LaTeX
Printed by Chalmers digital printing
Gothenburg, Sweden 2026

Numerical Modelling of High Harmonic Generation in Gases
Linus Hagedorn
Department of Subatomic, High Energy and Plasma Physics
Chalmers University of Technology

Abstract

High harmonic generation is a highly nonlinear phenomenon produced in high-intensity laser-matter interactions, which results in the emission of wideband light in the extreme-ultraviolet or soft X-ray spectrum. The emitted light consists of harmonics – spectral peaks at integer multiples of the frequency of the driving laser. The intensity of the generated harmonics is approximately constant over a wide range of frequencies, yielding a wideband spectrum and high frequency emission. The large bandwidth together with the coherence of the emitted light leads to the generation of attosecond duration pulses that have applications in measuring physical systems with ultrafast dynamics, such as that of electrons in atoms and molecules.

Due to the highly nonlinear and quantum-mechanical nature of high harmonic generation, the theoretical modeling of high harmonic generation must include single atomic responses in the presence of laser light as well as nonlinear wave propagation equations. This requires numerical simulations in order to calculate quantities relevant for experiments, such as conversion efficiency and the harmonic spectrum.

In this work, a numerical simulation code called HarP has been developed to simulate high harmonic generation in gases. The code utilizes the Crank-Nicolson numerical scheme to solve the wave propagation equations and combines theoretical models and tabulated data for the microscopic response of the atoms. This approach reduces computational cost compared with non-tabulated approaches and complexity while maintaining accuracy. To validate HarP, benchmarks were performed against another high-harmonic code utilizing a different methodology, as well as against established simulation results from the literature. More specifically, these benchmarks focus on ionisation rates, pulse profiles for different pressures and propagation lengths, and conversion efficiencies in argon. The result demonstrates overall good agreement for ionisation, laser pulse propagation, and conversion efficiency, with only minor differences observed.

Keywords: High-harmonic generation, Numerical simulation, Attosecond Science

Acknowledgements

This project would not have been possible without the support of many wonderful people.
First, I would like to express my gratitude to my supervisor, Dr. Dominika Maslárová, for her guidance and for helping me navigate and understand this field. Her willingness to engage in thoughtful conversations whenever I had questions truly helped drive this project forward. I am also very grateful that she provided the MMA simulations used to benchmark HarP.

I would also like to thank Prof. Tünde Fülöp for giving me the opportunity to pursue this project in the first place and for welcoming me into the group as a research assistant. Her support made it possible for me to travel to Lund to discuss the underlying science and tour their facilities, for which I am extremely grateful.

Furthermore, I would like to thank Robin Weissenbilder. I really appreciate him taking the time to meet with me, patiently answering my questions about HHG, and providing several of the tables used in this work.

I would also like to thank István Pusztai and Sarah Newton for carefully reading this thesis and providing valuable feedback and suggestions that helped improve its quality and clarity.

Finally, to the wonderful members of the plasma group: thank you for taking me in and for all the great conversations over fika as well as for going bouldering together.

Linus Hagedorn, Gothenburg, June 2026

Contents

1 Introduction **1**

2 Theoretical background **4**
2.1 Macroscopic picture 4
2.1.1 Propagation of fundamental and harmonic fields 5
2.1.2 Free currents 7
2.1.3 Boundary conditions 7
2.1.4 Polarisation density and microscopic connection 9
2.1.5 Phase mismatch 11
2.2 Microscopic picture 11
2.2.1 Susceptibilities and absorption 11
2.2.2 Three-step model 12
2.2.3 Lewenstein Model 13
2.3 Ionisation 15
2.3.1 PPT-model 15

3 Code structure **18**
3.1 Propagation module 18
3.2 Ionisation module 20
3.3 MMA module 22
3.4 Plotting module 22

4 Results **23**
4.1 Stability 23
4.1.1 Energy conservation 23
4.1.2 Intensity profile comparisons 25
4.2 Ionisation 26
4.3 Harmonic generation 28
4.3.1 Conversion efficiencies 29

5 Discussion **30**
5.1 Outlook 32
5.2 Conclusions 33

A Appendix **37**
A.1 Derivation of the Helmholtz equation in HHG 37
A.2 Derivation of dynamic polarizability from scattering theory 39
A.3 Derivation of Crank-Nicolson scheme 40

A.3.1 Boundary conditions 41

1
Introduction

Lasers have become a foundational technology since their first realization in 1960 using ruby crystal [1], opening up opportunities for a plethora of applications in both science and society at large. As achievable laser intensities continuously increased over the years, new optical phenomena could be observed when high-intensity laser light impinged on different media. Some of these phenomena are highly nonlinear and could, for example, change the wavelength of the outgoing light, leading to new discoveries in nonlinear optics. One such phenomenon that was first observed in the 1980s is called high harmonic generation (HHG) [2, 3].

Imagine playing an instrument, such as a flute or a violin. When playing a specific note, the sound the instrument makes does not only contain one specific frequency but a range of other frequencies, mostly harmonics of the ground tone, so called overtones. This is the result of nonlinearities arising when the sound is produced. Similarly a nonlinear optical system can generate overtones but with laser light instead. More specifically, HHG is the emission of light which contains harmonic frequencies (overtones) of the incoming laser light. Moreover, these harmonics are similar in intensity over a wide range of harmonic orders followed by a sharp cut-off in intensity. In particular, the wide range of harmonic orders lead to high harmonics of relatively high intensity in the soft X-ray spectrum. This source of wideband radiation was essential to the discovery of experimental schemes to generate attosecond pulses. As the name suggests, attosecond pulses have a duration in the attosecond range, making them excellent for the study of electrons in atoms. The development of such techniques revolutionized ultrafast science and ultimately led to the awarding of the 2023 Nobel Prize in Physics to Anne L'Huillier, Pierre Agostini, and Ferenc Krausz for their contribution to attosecond science and HHG.

To theoretically describe the HHG process, a coupled system consisting of a nonlinear electromagnetic wave equation and the time dependent Schrödinger equation (TDSE) must be solved. The electromagnetic wave equation itself, describes the propagation of the harmonic and fundamental fields in the HHG process. The TDSE in turn, describes the single-atom response from these fields. The coupling between the TDSE and the nonlinear wave equation is through two variables: the electric field which couples the wave equation to the TDSE, and a source term in the wave equation which couples the single-atom response from the TDSE to the wave equation. For modeling such a system, the solution can be done numerically using computer simulations. One example of such a simulation approach is the modular multiscale approach (MMA) [4], which uses the coupled system to simulate the propagation of the driving laser pulse, the generation of harmonics, and their propagation. More specifically, MMA solves the coupled system by iteratively solving each of the equations in a loop. The loop consists of two main steps: first, the electric field is propagated one step forward and input into the TDSE to calculate the single-atom response; second, the subsequent single-atom response is used for the next step of the electric field propagation.

A more lightweight alternative is to take a tabulated TDSE approach, which uses tables for the single atom response and additional approximations in order to solve the nonlinear wave equation through direct discretization by using a Crank-Nicolson scheme [5–7]. This lightweight approach enables fast simulations over a large set of conditions while still proving to be reasonably accurate in most experimentally relevant cases. The tabulated nature also allows for the possibility of running fast simulations using data from the three-dimensional Schrödinger equation, thus incorporating additional effects due to the increased dimensionality.

In the context of this work, a code using tabulated data for the time dependent Schrödinger equation has been developed, called Harmonic Propagation (HarP). The aim of this thesis is therefore to develop HarP and describe its structure. The difference in approach and complexity between MMA and HarP is significant, which in combination with the nonlinearity of the HHG process makes benchmarking between these two codes non-trivial.

The system that HarP models is conceptually very simple. First, a driver laser pulse is generated and propagated towards a chamber filled with gas. Then, as the pulse travels through the gas, it generates harmonics that also propagate through the chamber, resulting in partial phase mismatch between the laser pulse and harmonics. Finally, the pulse and harmonics propagate towards a detector placed along the z-axis, at a distance from the gas chamber's entrance. This system is illustrated in Fig. 1.1.

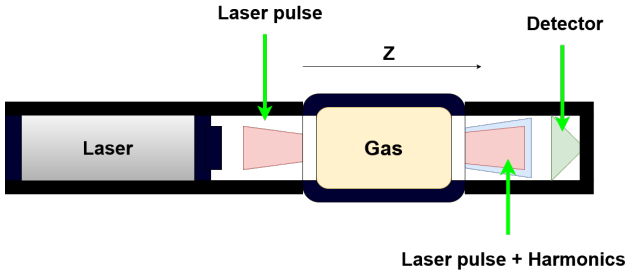

Figure 1.1: Schematic image of the setup HarP models. The initial pulse in red propagates through the gas (yellow), resulting in a pulse with harmonics (red+blue). The harmonic pulse is then detected by the detector (green), where z is the propagation axis.

Since HarP uses a precalculated tabulated TDSE approach, the choice of gas and laser wavelength is fixed to the data for a specific element and incoming laser wavelength. In this work, the tables used provide data for argon with a laser wavelength of 810 nm. However, note that the algorithms developed are themselves more general, and may be used with different data.

The following sections will describe the theory regarding HHG, the code structure of HarP, the simulation results with given tables, and the conclusions. More specifically, section 2 is divided into two primary parts: a part describing the macroscopic aspects and a section describing the microscopic theory of HHG. In the macroscopic part, the electromagnetic propagation equation and the connection to the microscopic models via the source term are discussed. An explanation of macroscopic variables such as laser intensity, gas density, and phase mismatch is also provided. The microscopic part describes the single atom response, the microscopic relations behind optical properties such as refractive index and susceptibility, and the theory regarding strong-field ionisation. Section 3 details the code structure of HarP and the purpose, as well as the function of, the different modules included in HarP. Section 4 contains the simulation benchmarks, stability tests, and other

results. Lastly, in section 5 we draw the conclusions from the results, a discussion about the causes behind the differences observed, and outline further avenues for future investigations.

2

Theoretical background

High harmonic generation (HHG) is a process where matter interacts with a high-intensity laser field. HHG results in the emission of electromagnetic radiation at multiples of the laser frequency, referred to as the fundamental frequency. In gases, the macroscopic theoretical description of HHG falls within the framework of nonlinear optics, where only odd harmonics are generated as a consequence of the so-called inversion symmetry [8, Sec. 13.6][9]. Also, according to classical nonlinear optics, the intensities of such harmonics are expected to drop off exponentially as a function of frequency [8, Sec. 13.4] [10]. However, due to the special form of the nonlinearity that appears in HHG settings, the generated harmonics plateau in intensity over a wide range of harmonics. Such a plateau allows for the generation of very spectrally broad light of high intensity, leading to the possibility of generating pulses which are very narrow temporally, in attosecond pulse trains. Since HHG is a highly nonlinear effect, the scales at which subprocesses are accurately and efficiently described differ significantly. Due to this, the theory describing such a process can be roughly divided into two parts: a macroscopic part, which deals with the propagation of fundamental and harmonic fields through the lens of electromagnetism as well as nonlinear optics, and a microscopic part dealing with the atomic response in the presence of a strong electromagnetic field with semiclassical or quantum mechanical models.

2.1 Macroscopic picture

The macroscopic properties of the highly nonlinear HHG process can be described using nonlinear optics. The importance of HHG in the generation of attosecond pulse trains could be illustrated using the Heisenberg-Gabor limit [11], which sets a lower bound on the product of the spectral bandwidth $\Delta\omega$ and temporal bandwidth Δt as

$$\Delta\omega\Delta t \geq \frac{1}{2}. \tag{2.1}$$

A relation is therefore enforced between the conjugate variables frequency and temporal width. Thus, if we would like to have very narrow pulses in time ($\Delta t \simeq 10^{-18}$ s), the corresponding spectral range required would have to be very wide, which HHG allows[1].

To understand the overall propagation of the fundamental and generated harmonic fields, the Helmholtz equation can be used, which is introduced in the next subsection.

[1]Note that the wideband nature alone does not guarantee very short pulses; it requires the components to have a specific phase relation. Recall, that white noise and a Dirac delta pulse share the same amplitude spectrum.

2.1.1 Propagation of fundamental and harmonic fields

In this section, we follow the derivation done by Anne L'Huillier et.al. [6] in combination with derivations done by Robin Weissenbilder in his PhD thesis [12].

The propagation of fundamental and harmonic fields is modelled by the wave equation in a dielectric medium. In the context of this work and for the derivation of the final propagation equation, it is assumed that the ionisation of the medium is low, resulting in the neglect of free currents (i.e. currents carried by free electrons). It is also assumed that the medium is a non-magnetic material [8, Sec. 2.1]. Given this, the propagation is determined by

$$\left(\nabla^2 - \frac{1}{c^2}\frac{\partial^2}{\partial t^2}\right)\boldsymbol{E}(r,t) = -\frac{1}{\varepsilon_0 c^2}\frac{\partial^2}{\partial t^2}\boldsymbol{P}(r,t), \tag{2.2}$$

where c is the speed of light, ε_0 is the vacuum permittivity, $\boldsymbol{P}(r,t)$ is the general polarisation density and $\boldsymbol{E}(r,t)$ is the electric field, both of which depend on the radial coordinate r as well as time t. For nonlinear processes, the polarisation density $\boldsymbol{P}(r,t)$ in Eq. (2.2) can be split as a sum of a linear contribution $\boldsymbol{P}^L$ and nonlinear contribution $\boldsymbol{P}^{NL}$, resulting in

$$\left(\nabla^2 - \frac{1}{c^2}\frac{\partial^2}{\partial t^2}\right)\boldsymbol{E}(\boldsymbol{r},t) = -\frac{1}{\varepsilon_0 c^2}\frac{\partial^2}{\partial t^2}\left(\boldsymbol{P}^L(\boldsymbol{r},t) + \boldsymbol{P}^{NL}(\boldsymbol{r},t)\right). \tag{2.3}$$

In order to describe the propagation of harmonics, a number of approximations are employed [6]. Firstly, the slowly varying envelope approximation (SVEA) is adopted, resulting in the separation of the pulse profile (envelope) from the rapid oscillations of the actual field. Since the pulse envelope can be separated from the fast oscillations, the electric field and polarisation density of a certain harmonic can be approximated as the product of an envelope function and an oscillating term at the wavenumber $k_{q0} = qk_1$ for the polarisation density and $k_q = qk_1 n_q$ for the electric field, where q represents the harmonic number, n_q is the refractive index for a harmonic q, and $k_1 = 2\pi/\lambda_1$ is the wavenumber for the fundamental field with a wavelength λ_1. More explicitly, the electric field $\boldsymbol{E}_q$ and the nonlinear polarisation density $\boldsymbol{P}_q^{\mathrm{NL}}$ for a specific harmonic q can be approximated by

$$\boldsymbol{E}_q(\boldsymbol{r},t) = \bar{\boldsymbol{E}}_q(r,z,t)e^{ik_q z}, \tag{2.4}$$

$$\boldsymbol{P}_q^{NL}(\boldsymbol{r},t) = \bar{\boldsymbol{P}}_q^{NL}(r,z,t)e^{ik_{q0} z}, \tag{2.5}$$

where $\bar{\boldsymbol{E}}_q(r,z,t), \bar{\boldsymbol{P}}_q^{NL}(r,z,t)$ are the respective envelope functions of $\boldsymbol{E}_q(r,t)$ and $\boldsymbol{P}_q^{NL}(r,t)$. Secondly, the paraxial approximation is assumed, where the propagation of harmonic radiation is expected to occur mostly along the propagation axis z. The paraxial approximation states that the evolution of the field is mostly done in the direction parallel to the propagation axis, so only the wave vector along the propagation direction is considered. This results in

$$\frac{\partial^2}{\partial z^2} \ll 2ik_q\frac{\partial}{\partial z}, \tag{2.6}$$

thus terms containing $\frac{\partial^2}{\partial z^2}$ acting on the envelope functions can be neglected. Assuming that the setup seen in Fig. 1.1 is cylindrically symmetric, the dependence on the azimuthal angle can be neglected.

Using cylindrical symmetry, the SVEA together with the paraxial approximation on the propagation equation in (2.3), leads to the paraxial inhomogeneous Helmholtz equation describing the

macroscopic evolution of the harmonic field [2]

$$\left(2ik_{q0}\frac{\partial}{\partial z}+\frac{\partial^2}{\partial r^2}+\frac{1}{r}\frac{\partial}{\partial r}+2k_{q0}\Delta k_q\right)\bar{\boldsymbol{E}}_q=-\frac{k_{q0}^2}{\varepsilon_0}\bar{\boldsymbol{P}}_q^{NL}. \tag{2.7}$$

This equation is the primary equation used for the macroscopic propagation of specific harmonics in HarP [3]. In equation (2.7), Δk_q describes the phase mismatch between the polarisation density and the electric field for a certain harmonic q, while $\bar{\boldsymbol{P}}_q^{NL}$ is the nonlinear polarisation density envelope for the same harmonic which acts as a source for the generated harmonic. The phase mismatch Δk_q in equation (2.7) creates destructive interference and decoherence of the harmonics, leading to significant losses. By investigating the different parameters that affect the phase mismatch, one can find theoretical conditions where the harmonic yield is maximised for a given laser field in terms of a conversion efficiency.

Two such parameters are the pressure of the gas p, which affects the overall number density of the medium, and the length of the medium l over which the laser propagates. As investigated in Refs. [7, 13], the values of p and l that maximise the conversion efficiency lie on a hyperbola. Thus, the maximum yield follows the relation

$$pl=b, \tag{2.8}$$

where b is a constant and it essentially represents the integrated number density of the medium along the propagation. The conversion efficiency η can be determined by the ratio between the energy of the fundamental and harmonic field. This can be done by integrating the intensity of the electric field $\boldsymbol{I}$ defined as

$$I=\frac{1}{2}c\varepsilon_0|\bar{\boldsymbol{E}}|^2, \tag{2.9}$$

for the electric field envelope $\bar{\boldsymbol{E}}$ [14, Eq. 8-85]. Going from Cartesian coordinates x, y, z to cylindrical coordinates r, θ, z, the energy is calculated as

$$H=\int\int\int I(x,y,z,t)\;dx\;dy\;dt=\int d\theta\int\int rI(r,z,t)\;dr\;dt\longleftrightarrow\quad\pi c\varepsilon_0\int\int r|\bar{\boldsymbol{E}}(r,z,t)|^2\;dr\;dt,$$

where H is the total energy of the electric field $\boldsymbol{E}(r,z,t)$ at some fixed z. From this, the conversion efficiency for a specific harmonic is calculated as

$$\eta=\frac{\int\int r|\bar{\boldsymbol{E}}_q(r,t)|^2\;dr\;dt}{\int\int r|\bar{\boldsymbol{E}}_1(r,t)|^2\;dr\;dt}, \tag{2.10}$$

where $\bar{\boldsymbol{E}}_q(r,t)$ is the harmonic field envelope and $\bar{\boldsymbol{E}}_1(r,t)$ is the fundamental field envelope. As an efficiency, it shows how much of the energy in the fundamental field is converted to a specific harmonic field $\boldsymbol{E}_q(r,t)$ and is a number between 0 and 1.

Since the fundamental field is not generated by harmonic generation and that the conversion efficiency η is small, the source in equation (2.7) must be zero for the fundamental field. Thus, the macroscopic propagation equation for the fundamental field becomes

$$\left(2ik_1\frac{\partial}{\partial z}+\frac{\partial^2}{\partial r^2}+\frac{1}{r}\frac{\partial}{\partial r}+2k_1\Delta k_1\right)\bar{\boldsymbol{E}}_1=0. \tag{2.11}$$

[2] For an in-depth derivation of the paraxial inhomogeneous Helmholtz equation used, see appendix A.1.

[3] For a specific derivation of the equations implemented in the simulation code, see A.3

2.1.2 Free currents

When free currents are not neglected, the resulting propagation equations (2.7) and (2.11) include a free current term $\boldsymbol{J}_{q,\text{free}}$ for all harmonic and fundamental fields q. In HHG, free currents arise primarily from a flow of free electrons in the medium as a consequence of ionisation [4]. In the macroscopic Helmholtz Eq. (2.3), although neglected in this work, they would contribute to the source term by $-i\omega_q \bar{\boldsymbol{J}}_{q,\text{free}}$, where $\bar{\boldsymbol{J}}_{q,\text{free}}$ is the envelope function of the free current $\boldsymbol{J}_{q,\text{free}}$ [4]. The omission of free currents in HarP is done on the basis that the ionisation is assumed to be low [7]. However, note that the MMA approach described in Ref. [4] does include free currents, displaying a difference in approximations.

2.1.3 Boundary conditions

In order to solve the propagation equation defined in Eqs.(2.7) and (2.11), appropriate boundary conditions are needed. In general, when solving partial differential equations (PDEs), there are two common types of boundary conditions: Neumann and Dirichlet conditions [15]. Neumann conditions state that the derivative of the solution function of the PDE $y(\boldsymbol{x})$ is defined by some function $f(\boldsymbol{x})$ at the boundary $\partial\Omega$ of some domain Ω with respect to the independent variable $\boldsymbol{x}$, providing a boundary that does not enforce a specific value of $y(\boldsymbol{x})$ and can be written as

$$\left.\frac{\mathrm{d}y(\boldsymbol{x})}{\mathrm{d}\boldsymbol{n}}\right|_{\boldsymbol{x}=\boldsymbol{x}'} = f(\boldsymbol{x}'),\ \forall \boldsymbol{x}' \in \partial\Omega, \tag{2.12}$$

where $\boldsymbol{n}$ is the normal vector of the boundary $\partial\Omega$.

Dirichlet conditions, on the other hand, specify the value of the solution directly on the boundary, thus fixing the value. More formally, the Dirichlet condition could be written as

$$\left.y(\boldsymbol{x})\right|_{\boldsymbol{x}=\boldsymbol{x}'} = f(\boldsymbol{x}'),\ \forall \boldsymbol{x}' \in \partial\Omega, \tag{2.13}$$

where the specific value of the solution $\boldsymbol{y}$ is fixed according to the specified function $f(\boldsymbol{x})$ on the boundary.

In the context of this work, Eqs. (2.7) and (2.11) need a total of two boundary conditions and one incoming boundary condition in order to be solved numerically: One for the electric field envelope $\boldsymbol{E}_q(r=0,t,z)$ at $r=0$, one at some maximum radius $r=r_{\max}$ as $\boldsymbol{E}_q(r=r_{\max},t,z)$, and lastly one incoming boundary condition describing the initial distribution $\boldsymbol{E}_q(r,t,z=z_{\text{start}})$ at $z=z_{\text{start}}$. Due to the similarities between Eq. (2.7) and Eq. (2.11), the boundary conditions are assumed to be the same between both equations where the only exception is in their respective incoming boundary conditions.

In order to determine the incoming boundary condition and the other two boundary conditions, one can motivate a certain choice depending on the experiment design or the underlying physics. Physically, if the boundary at $r=r_{\max}$ is either far transverse from the propagation axis in z or there is a wall in the experiment, the electric field envelope at that point is nearly or exactly zero. Thus, the chosen boundary condition for $\boldsymbol{E}_{q,1}(r=r_{\max},t,z)$ becomes a Dirichlet condition where $f(\boldsymbol{x})=0$. Moreover, since the profile of the envelope is continuous at $r=0$ and the propagation equation exhibits cylindrical symmetry, Neumann conditions are chosen such that the normal derivative is

set to zero in Eq. (2.12). Since the cylindrical geometry is used, the normal vector of the cylindrical domain points along the radial direction. Thus, the specific Neumann condition used is that the radial derivative of the electric field is set to zero. Lastly, the incoming condition at $z = z_{\text{start}}$ seems at first glance rather arbitrary since this condition represents the envelope of the pulse before propagating in the medium, which is different for the fundamental and harmonic fields. Since the fundamental field is assumed to propagate in vacuum before hitting the gas, the generation of harmonics is nonexistent, leading to a Dirichlet condition with $f(\boldsymbol{x}) = 0$ at $z = z_{\text{start}}$ for the propagation equation in Eq. (2.7). As for the fundamental field envelope $\boldsymbol{E}_1(r, t, z = z_{\text{start}})$ in Eq.(2.11), it is assumed to take a Gaussian form as its incoming condition [16]

$$\begin{aligned}\bar{\boldsymbol{E}}_1(r,t,z)\Big|_{z=z_{\text{start}}} = \boldsymbol{E}_0 \frac{b_0}{b(z_{\text{start}})} \exp\Bigg[&- \left(\frac{r}{b(z_{\text{start}})}\right)^2 - 2\ln(2)\left(\frac{t}{t_{\text{FWHM}}}\right)^2 \\ &+ i\left(\phi_{\text{Gouy}}(z_{\text{start}}) - \frac{k_1 r^2}{2R(z_{\text{start}})}\right)\Bigg],\end{aligned} \tag{2.14}$$

where $\boldsymbol{E}_0$ is the maximum electric field strength of the envelope, b_0 is the beam waist of the pulse at its focus, $b(z)$ is the beam radius representing the value where the field strength is $1/e$ of its axial value, t_{FWHM} is the duration of the pulse at full width half maximum (FWHM) of the intensity, ϕ_{Gouy} is the Gouy phase for the pulse, and $R(z)$ is the radius of the curvature of the wavefronts. The definitions of all of these variables are

$$\begin{aligned} b_0 &= \sqrt{\frac{\lambda_1 z_r}{\pi}}, \\ b(z) &= b_0\sqrt{1 - \frac{z^2}{z_r^2}}, \\ R(z) &= \frac{z^2 + z_r^2}{z}, \\ \phi_{\text{Gouy}} &= \arctan\left(\frac{z}{z_r}\right), \end{aligned}$$

where λ_1 is the wavelength of the fundamental field, and z_r is the Rayleigh length, describing the length along the propagation axis at which a beam doubles its cross-section area.

To summarize and formalize all the boundary conditions, the chosen boundary conditions used in the code for solving Eqs. (2.7) and (2.11) becomes:

$$\boldsymbol{E}_{q,1}(r,t,z)\Big|_{r=r_{\max}} = 0, \tag{2.15}$$

$$\frac{\partial \boldsymbol{E}_{q,1}(r,t,z)}{\partial r}\Big|_{r=0} = 0. \tag{2.16}$$

Although, the initial condition for the fundamental field envelope is defined, the initial condition for the harmonic field envelope used could subsequently be defined as

$$\boldsymbol{E}_q(r,t,z)\Big|_{z=z_{\text{start}}} = 0. \tag{2.17}$$

With the boundary conditions defined, they can directly be used in the code as described in A.3.

2.1.4 Polarisation density and microscopic connection

When referring to linear and nonlinear contributions of the polarisation density, the distinction is based on whether the polarisation depends linearly or nonlinearly on the electric field [8, Sec. 1.1]. Hence, $\boldsymbol{P}^{\mathrm{L}}$ can in general take the following form

$$\boldsymbol{P}^{L}(r,t) = \varepsilon_0 \chi^{(1)} \boldsymbol{E}(r,t), \tag{2.18}$$

where $\chi^{(1)}$ is the linear susceptibility of the medium [14, 17]. Usually in the context of nonlinear optics, the total polarisation density can be expanded in terms of perturbation theory [8, Sec. 1.1]

$$\boldsymbol{P}(r,t) = \varepsilon_0(\chi^{(1)}\boldsymbol{E} + \chi^{(2)}\boldsymbol{E}^2 + \chi^{(3)}\boldsymbol{E}^3 \dots), \tag{2.19}$$

with exponentially decreasing higher order perturbations $\chi^{(s)}$ where $s \in \mathbb{N}$. However, the exponential decrease of these perturbations suggests that the amplitude of the generated harmonics is also rapidly decreasing as a function of harmonic number [10]. This is in contradiction with experiments [18] where an initial decrease is observed as described by nonlinear optics, but the amplitude plateaus over a large range of harmonics. The quantitative explanation for this is that the perturbation expansion assumes the electron is being continually bound to the atom [19], which is not the case for HHG. Instead of using a perturbative approach in order to describe the nonlinear polarisation density, one could, from microscopic models of HHG, describe the nonlinear polarisation density in terms of the induced dipole moment. The underlying assumption here is that contributions from other moments, such as the quadrupole moment, are negligible, which is called the dipole approximation. Generalising the connection between the nonlinear polarisation density and the induced dipole moment in Ref. [6] for a general electric field, the expression becomes

$$\bar{\boldsymbol{P}}_q^{NL} = 2\mathcal{N}_a d_q e^{q\phi(E_1)}, \tag{2.20}$$

where d_q is the component of the induced dipole moment from a fundamental field with amplitude $|E_1|$ and oscillates at a frequency $q\omega$, $\mathcal{N}_a$ is the atomic density of neutral atoms (neutrals), and $\phi(E_1)$ is the phase of the fundamental field. The factor of 2 arises due to the specific convention used when Fourier expanding to $\boldsymbol{P}_q^{\mathrm{NL}}$ [4]. The dipole moment as shown in (2.20) could be split in terms of the dipole amplitude and phase. The corresponding phases and amplitudes for the dipole moment are calculated using the single active electron approximation (SAEA)[5], resulting in an extra factor of 2 as a consequence of spin degeneracy. Taking all of these effects into account, the dipole moment takes the form

$$d_q = 2|d_q^{\mathrm{SAEA}}|e^{i\arg(d_q^{\mathrm{SAEA}})}, \tag{2.21}$$

which when inserted into (2.20) results in

$$\bar{\boldsymbol{P}}_q^{NL} = 4\mathcal{N}_a|d_q^{\mathrm{SAEA}}|e^{i(\arg(d_q^{\mathrm{SAEA}})+q\phi(E_1))}, \tag{2.22}$$

where $\mathcal{N}_a$ is the number density of neutral atoms (neutrals), $\phi(E_1)$ is the phase of the fundamental field, and d_q^{SAEA} is the induced dipole moment from a single atom in the presence of a strong electric field using the single active electron approximation. The expression in (2.22) is used in the code in conjunction with precalculated tables for $|d_q^{\mathrm{SAEA}}|$ and $\arg(d_q^{\mathrm{SAEA}})$.

In the context of HHG, the linear susceptibility $\chi^{(1)}$ can be split into an atomic susceptibility χ_{at} and an electronic susceptibility χ_e respectively [6, 20]. The split comes from the specific effects

[4] It comes from the derivation of the propagation equation where $\boldsymbol{P}^{\mathrm{NL}}(t) = \frac{1}{2}\sum_q \boldsymbol{P}_q^{NL} e^{-i\omega q t} + \mathrm{c.c}$

[5] A detailed description of this approximation is found in section 2.2.2, describing the three step model.

occurring in the microscopic process, such as atomic interference and the creation of plasma. These susceptibilities can then be modelled separately by considering the microscopic picture, which is described below. Thus, the linear polarisation density in Eq.(2.18) can be expanded as

$$\boldsymbol{P}^{\mathrm{L}}(r,t) = \varepsilon_0 \left(\chi_e + \chi_{\mathrm{at}}\right) \boldsymbol{E}(r,t). \tag{2.23}$$

Even though the perturbative expansion is invalid since the electron is leaving the atom, the linear polarisation density is still valid since the divergence is due to the nonlinear polarisation. Thus, the approach of splitting the polarisation vector into a linear and nonlinear contribution is still valid. In general, the relation between the susceptibility χ and the refractive index of the medium n is

$$n = \sqrt{1+\chi}, \tag{2.24}$$

which, assuming $\chi = \chi^{(1)}$ and given the splitting of the susceptibility into an atomic and an electronic part, becomes

$$n = \sqrt{1+\chi_e+\chi_{\mathrm{at}}}. \tag{2.25}$$

Before the laser propagates in the medium, there is no plasma created, leading to the initial number density of neutrals becoming the number density of the medium. This is given by the ideal gas law, as

$$\mathcal{N}_{a0} = \frac{p}{k_b T}, \tag{2.26}$$

where p is the medium pressure, k_b is Boltzmann's constant, T is the temperature, and $\mathcal{N}_{a0}$ is the initial number density of neutrals. But as the laser pulse propagates through the medium, it ionises, changing the number density of neutrals and creating a number density of free electrons $\mathcal{N}_e$. To model this macroscopically, a rate equation can be used

$$\frac{\mathrm{d}}{\mathrm{d}t}\mathcal{N}_a(t) = -w\mathcal{N}_a(t), \tag{2.27}$$

where w is the ionisation rate as a consequence of the intense laser field, and $\mathcal{N}_a(t)$ is the time-dependent number density of neutrals with initial condition $\mathcal{N}_a(t=0) = \mathcal{N}_{a0}$. Since the total number density never changes, the number density of free electrons can be calculated as

$$\mathcal{N}_e(t) = \mathcal{N}_{a0} - \mathcal{N}_a(t), \tag{2.28}$$

Solving the update Eq. (2.27) with the initial condition $\mathcal{N}_a(t=0) = \mathcal{N}_{a0}$ gives

$$\mathcal{N}_a(t) = \mathcal{N}_{a0} e^{-\int_0^t w \mathrm{d}t}, \tag{2.29}$$

where the solution is used in the code to update the number densities [6]. Since the ionisation rate is dependent on the underlying atomic structure for a specific element, it needs to be modelled microscopically using models such as the Perelomov, Popov and Terent'ev (PPT)-model [21, 22] or by numerical calculations of the time-dependent Schrödinger equation (TDSE). When looking at the Eqs. 2.22, 2.23, 2.25, and (2.27) the coupling between the macroscopic and microscopic picture becomes apparent since $\chi_{\mathrm{at}}, \chi_e$, d_q^{SAEA}, and w are quantities that need to be modelled microscopically.

[6] For the specific expression used, see Eq. (3.6)

2.1.5 Phase mismatch

In the macroscopic picture, the phase mismatch Δk_q is defined through the mismatch between the polarisation density phase and the phase of the electric field [6]. Looking at the phases in the expansions (2.4) and (2.5), the phase mismatch is defined as

$$\Delta k_q = k_q - qk_1, \tag{2.30}$$

where $k_q = n_q q k_1$. Factoring out the wave number of the fundamental and using the expression for the refractive index in (2.25), the phase mismatch becomes

$$\Delta k_q = \left(\sqrt{1 + \chi_{\text{at}} + \chi_e} - 1\right) k_{q0}, \tag{2.31}$$

where χ_{at} and χ_e are the atomic as well as electronic susceptibilities. The final expression in (2.31) is used in HarP. The phase mismatch occurs due to several different phenomena and can be thought of as a sum of individual phase mismatches due to these phenomena.

2.2 Microscopic picture

As seen from the macroscopic description of harmonic generation, the models describing the macroscopic behaviour of HHG point to underlying variables that need to be modelled microscopically. Such variables can be modelled in two primary ways: 1) variables that could be modelled without a microscopic model of the HHG process itself but require other microscopic descriptions, and 2) variables that need a microscopic model of the HHG process.

2.2.1 Susceptibilities and absorption

Considering susceptibilities and the absorption terms in the refractive index (2.25), the models used to describe such processes are separate from the HHG process in the sense that they are described from models in optics, plasma physics and scattering theory, thus being variables of the first type.

The electronic susceptibility models the inclusion of plasma in the medium, affecting the refractive index [14]. If plasma creation were the only effect, the refractive index experienced by the q-th harmonic could be described by

$$n_{\text{plasma},q} = \sqrt{1 - \frac{\mathcal{N}_e}{\mathcal{N}_{\text{p}}}}, \tag{2.32}$$

where $\mathcal{N}_{\text{p}} = m_e \varepsilon_0 \omega_q^2 / e^2$ is the critical plasma density and $\mathcal{N}_e$ is the density of free electrons [17, Sec. 7.5]. If compared with the general expression for the refractive index in (2.24), the electronic susceptibility could be seen as

$$\chi_e = -\frac{\mathcal{N}_e}{\mathcal{N}_p} \longleftrightarrow \chi_e = -\frac{\mathcal{N}_e e^2}{m_e \varepsilon_0 \omega_q^2},$$

where e is the electron charge, m_e is the mass of the electron, and $\omega_q = q\omega_0$ is the frequency of the harmonic in vacuum. Thus, the final electronic susceptibility becomes

$$\chi_e = -\frac{\mathcal{N}_e e^2}{m_e \varepsilon_0 \omega_q^2}. \tag{2.33}$$

From the expansion in equation (2.23), the atomic contribution to the polarisation density in the case of the q-th harmonic becomes

$$\boldsymbol{P}^{L}_{q,\mathrm{at}} = \varepsilon_0 \chi_{\mathrm{at}} \boldsymbol{E}_1, \tag{2.34}$$

where $\boldsymbol{E}_1$ is the electric field of the fundamental, χ_{at} is the susceptibility associated with

$$\boldsymbol{P}^{L}_{q,\mathrm{at}} = \mathcal{N}_a \boldsymbol{d}_q, \tag{2.35}$$

and by using the definition of the dynamic polarisability as

$$\boldsymbol{d}_q = \alpha_q \boldsymbol{E}_q, \tag{2.36}$$

the resulting susceptibility becomes

$$\chi_{\mathrm{at}} = \frac{\mathcal{N}_a \alpha_q}{\varepsilon_0}, \tag{2.37}$$

where α_q is the dynamic polarisability for a harmonic q and $\mathcal{N}_a$ is the atomic number density of neutrals [20]. The intuition of this equation is that when looking at a single atomic system, the optical response is α_q/ε_0, which is then scaled up by including the number density of neutrals. Now, there are two general ways of looking at the dynamic polarisability from a modelling perspective. Either one could use tabulated values for specific harmonics, or one could model the polarisabilities in terms of the atomic scattering theory and use tabulated values for the real scattering factors [23]. In terms of scattering theory, the polarisability could be determined by the two frequency-dependent scattering factors f_1 and f_2 as [7]

$$\alpha_q = \frac{r_e \varepsilon_0 \lambda_q^2}{\pi}(f_1 + i f_2)\left(\frac{n_a r_e \lambda_q^2}{4\pi}(f_1 + i f_2) + 1\right), \tag{2.38}$$

where r_e is the classical electron radius and λ_q is the wavelength of the q-th harmonic emission. The absorption of the medium comes from the complex contribution of the polarisability and is important for the harmonics, while for the typical fundamental wavelengths (800 nm), it becomes negligible. Thus, for the fundamental field $q = 1$, the dynamic polarisability reduces to the static polarisability α_0, which is a real element-specific quantity.

2.2.2 Three-step model

In order to get further insights into the microscopic response of the electron to high-intensity light, a semi-classical model called the three-step model can be used in the examination of HHG processes [19]. As the name suggests, the three-step model splits the HHG process into three distinct steps. Firstly, the separation of the electron wave packet from the atom is modelled through tunnelling of the mean atomic potential. Since the interactions with other dynamic electrons and atoms are extremely difficult to model and do not significantly contribute, the approximation of treating the atom and other electrons as static is made, the calculation is done in the presence of a time-independent potential. This approximation leads to the consideration of the dynamics of just one electron in the valence shell, the interaction of the static potential, and the interaction between the electric field and the electron wave packet. This approximation is known as the single active electron or (SAE) approximation, and can be more explicitly written as:

$$\mathcal{H}(t) = \mathcal{H}_0 + V(t), \tag{2.39}$$

[7] For a full derivation, see appendix A.2.

where $\mathcal{H}_0$ is the standard Hamiltonian of the atom and $V(t)$ is the potential from the electric field. Then, tunnelling could be done through the time-dependent Schrödinger equation for the wavefunction of the active electron $\psi(t)$ as

$$i\hbar\frac{\partial}{\partial t}\left|\psi(t)\right\rangle = \mathcal{H}(t)\left|\psi(t)\right\rangle, \tag{2.40}$$

alternatively, the tunnelling probability through an ionisation model such as PPT, where the probability of ionisation becomes the tunnelling probability. That is, the tunnelling probability $P(t)$ during an infinitesimal time dt can be modelled by

$$P(t) = w(E,\omega)dt, \tag{2.41}$$

where $w(E,\omega)$ is the ionisation probability and E is the magnitude of the electric field.

Secondly, after the tunnelling of the electron, the next step is the acceleration of the electron wave packet out from the atom. Since the electron path is considered to be classical, the entire path is modelled by Newton's equations, where the influence of the atomic potential is taken to be weak. The tunnelled electrons here are assumed to tunnel to the continuum at the ion position, and with an initial velocity of zero. More specifically, if the driving laser field is taken to be linearly polarised as $\mathrm{Re}(E(t)) = \mathcal{E}_0\cos(\omega_0 t)$, the dynamics of the tunnelled electron can be modelled as

$$m_e\frac{\partial^2}{\partial t^2}x(t,t_i) = e\mathcal{E}_0\cos(\omega_0 t), \tag{2.42}$$

from which the specific electron path $x(t,t_i)$ can be determined.
Lastly, in the third step, when the electric force on the electron changes the sign, the electron is accelerated back towards the atom, creating an oscillating dipole at odd harmonics of the driving lasers frequency through interference with the atom under the assumption of negligible depletion of the ground state. The oscillation of the dipole leads to the emission of harmonic radiation, which, due to the electron energy gained by the electromagnetic field from the laser when interfering with the atom, yields a wide range of different harmonics with a sharp cut-off at the energy

$$E_{max} = 3.17U_p + I_p, \tag{2.43}$$

where $U_p = e^2\mathcal{E}_0^2/4m_e\omega_0^2$ is the laser ponderomotive energy and I_p is the ionisation energy. The specific energy $3.17U_p$ stems from the maximum energy an electron can gain during its trajectory.

2.2.3 Lewenstein Model

In comparison to the three-step model, the Lewenstein model is a fully quantum mechanical model which treats the electron dynamics through an approximated Schrödinger equation. However, the Lewenstein model takes into account several quantum effects that the three-step model neglects [9, 24]. Such effects include diffusion of wave packets in the continuum state and quantum interference upon recombination. Although fully quantum mechanical in nature, the Lewenstein model uses the single active electron approximation, strong field approximation, and the neglect of the ground state depletion in order to simplify the N-body Schrödinger equation while keeping the relevant physics. Specifically, the physical system investigated is an isolated atomic system, neglecting correlations between atomic systems. Given such a system, it is also assumed that the profile of the laser field is strong compared to the atomic potential ($\boldsymbol{E}(t) \gg V(\boldsymbol{x})$), leading to a spatially constant electric field and a non-existent magnetic field. Moreover, the process is assumed to be non-relativistic and uses

the classical version of the gauge potential to account for the laser field. By the above assumptions, the Schrödinger equation becomes

$$i\hbar\frac{\partial}{\partial t}\left|\Psi(\boldsymbol{x},t)\right\rangle = \left(-\frac{\hbar^2}{2m_e}\nabla^2 + V(\boldsymbol{x}) - \boldsymbol{x}\cdot\boldsymbol{E}(t)\right)\left|\Psi(\boldsymbol{x},t)\right\rangle, \tag{2.44}$$

where $|\Psi(\boldsymbol{x},t)\rangle$ is the general state of the single electron in the valence shell, $V(\boldsymbol{x})$ is the atomic potential, $\boldsymbol{E}(t)$ is the electric field the atom experiences at the laser field, ∇^2 is the Laplacian, m_e is the electron mass, and $\hbar$ is the Dirac constant.

In order to solve the time-dependent Schrödinger equation in (2.44), the ansatz of a general electron state can be made as

$$\left|\Psi(t)\right\rangle = e^{\frac{-I_p t}{\hbar}}\left(a(t)\left|0\right\rangle + \int d^3\boldsymbol{k}\; b(t,\boldsymbol{k})\left|\boldsymbol{k}\right\rangle\right), \tag{2.45}$$

where $|\Psi(t)\rangle$ is the general state of the electron, $|0\rangle$ is the bound ground state for the electron, $|\boldsymbol{k}\rangle$ is the continuum state for the electron with momentum $\boldsymbol{k}$, I_p is the ground state energy, and $a(t)$ as well as $b(t,\boldsymbol{k})$ are the corresponding amplitudes for the states. By setting $a(t) \simeq 1$ and inserting the ansatz into the Schrödinger equation, one gets a differential equation which can be solved for $b(t,\boldsymbol{k})$. The reason why $a(t) \simeq 1$ is that the Lewenstein model assumes no depletion in the ground state, resulting in just a small electron population leaving the atom at each optical cycle of the laser field.

As described earlier, the coupling between the macroscopic and microscopic pictures in HHG is done through the induced dipole moment from the high-intensity laser light. In the Lewenstein model, the general dipole moment is calculated through the use of the time-dependent wave equations $|\Psi(t)\rangle$ and the position $\boldsymbol{x}$ by the equation

$$d(t) = \left\langle\Psi(t)\right|\boldsymbol{x}\left|\Psi(t)\right\rangle. \tag{2.46}$$

When looking at the ansatz made in equation (2.45), the state is split into two specific parts. One part describes the bound state of the electron $|0\rangle$ and one part describes the continuous state, which describes the free electron in the continuum $|\Psi_c(t)\rangle$. From this, a schematic expansion looks like

$$\left|\Psi(t)\right\rangle = \left|0\right\rangle + \left|\Psi_c\right\rangle, \tag{2.47}$$

and by using the expansion in equation (2.47) with the dipole expression in equation (2.46), the total dipole moment becomes:

$$d(t) = \left\langle 0\right|\boldsymbol{x}\left|0\right\rangle + \left(\left\langle\Psi_c\right|\boldsymbol{x}\left|0\right\rangle + \left\langle 0\right|\boldsymbol{x}\left|\Psi_c\right\rangle\right) + \left\langle\Psi_c\right|\boldsymbol{x}\left|\Psi_c\right\rangle, \tag{2.48}$$

where $\langle\Psi_a|\boldsymbol{x}|\Psi_b\rangle$ are the transition elements from a given state Ψ_a to a new state Ψ_b. Since HHG mostly occurs in the transition between bound and continuum states, as highlighted by the three-step model, the dipole moment can be calculated by only considering the bound-continuum transition states. Using this, the time-dependent dipole moment in a given direction $\boldsymbol{n}$ is calculated as

$$d(t) = i\int_0^t dt' \int d^3\dot{\boldsymbol{q}}\; \boldsymbol{n}\cdot\boldsymbol{d}_p^*(\dot{\boldsymbol{q}} - \boldsymbol{A}(t))\cdot\boldsymbol{E}(t')\exp(-iS(\dot{\boldsymbol{q}},t,t'))\boldsymbol{d}_p(\dot{\boldsymbol{q}} - \boldsymbol{A}(t')) + \text{c.c}, \tag{2.49}$$

where $\boldsymbol{d}_p$ is the bound-continuum transition element for the dipole, $\boldsymbol{A}(t)$ is the gauge field, $\boldsymbol{E}(t)$ is the electric field of the laser, $\dot{\boldsymbol{q}}$ is the canonical momentum, and $S(\dot{\boldsymbol{q}},t,t')$ is the quasi-classical action. The canonical momentum can be formulated as

$$\dot{\boldsymbol{q}} = \boldsymbol{k} + \boldsymbol{A}(t), \tag{2.50}$$

and the quasi-classical action is given by

$$S(\dot{\boldsymbol{q}}, t, t') = \int_{t'}^{t} dt'' \left(\frac{(\dot{\boldsymbol{q}} - \boldsymbol{A}(t''))^2}{2} + I_p \right). \tag{2.51}$$

In order to get the tabulated dipole moments used in the code, the dipole spectrum needs to be calculated. The dipole spectrum can be calculated by Fourier transforming the time-dependent dipole moment in equation (2.49) which, by using the result along with some calculations, results in the tabulated dipole moments. Note that, the three step model can be directly seen in the integral expression of Eq. (2.49) where $\boldsymbol{d}_p^*(\dot{\boldsymbol{q}} - \boldsymbol{A}(t))$ represent the first step, $\boldsymbol{E}(t') \exp(-iS(\dot{\boldsymbol{q}}, t, t'))$ the second, and $\boldsymbol{d}_p(\dot{\boldsymbol{q}} - \boldsymbol{A}(t'))$ the third. The results of doing these calculations is to procure the single atom response in terms of the induced dipole spectrum d_q as described in Eq. (2.21).

2.3 Ionisation

Since this section follows primary literature on PPT in atomic units (a.u), the expressions in this section are also written in terms of atomic units.

Due to the high-intensity laser light used in the HHG process, the medium ionises, leading to pulse shaping of the harmonics and fundamental field. The ionisation also contributes to the phase mismatch Δk_q of the generated harmonics as well as the nonlinear polarisation vector $\boldsymbol{P}_q^{NL}$. In turn, the increase of overall phase mismatch for the harmonics leads to an overall decrease in conversion efficiency, producing harmonics of much lower intensity. Thus, modelling the intensity-dependent ionisation rate becomes important in attosecond science. Depending on the frequency and intensity of the fundamental field, the dominant mechanism for the ionisation rate changes, leading to different ionisation regimes. In order to quantify the different regimes, the Keldysh parameter is introduced

$$\gamma = \frac{\omega \sqrt{2I_p}}{E_0}, \tag{2.52}$$

where I_p is the ionisation potential, ω is the laser angular frequency and E_0 is the maximum field strength of the fundamental field. Given the Keldysh parameter in (2.52), the ionisation rate can be divided into two separate regimes. For $\gamma \ll 1$, the ionisation is primarily dominated by the tunnelling of electrons in the ground state through the atomic potential. This is possible due to the electric field reducing the amplitude of the atomic potential, allowing the tails of the wavefunction to dip outside the potential barrier. On the other hand, for the region $\gamma \gg 1$, the effect of multi-photon absorption becomes dominant. In the multi-photon region, the electrons ionise through the process of absorbing several photons within the electron's relaxation time, giving it enough energy to overcome the atomic potential. However, the strength of the laser field in HHG usually falls in the tunnelling regime.

2.3.1 PPT-model

In order to model the intensity-dependent ionisation rate in the tunnelling regime ($\gamma \ll 1$), a semi-classical model is used called PPT [21, 22]. This model uses the time-dependent Schrödinger equation (TDSE) in order to solve for the wavefunction evolution. By calculating the wavefunction for a semi-classical Hamiltonian, the ionisation rate can be derived from the probability current going through a surface at infinity. The expression relating the ionisation rate and the probability current in the original paper is

$$w(E,\omega) = 2 \lim_{r\to\infty} \bar{J}(r,t) \tag{2.53}$$

where $w(E,\omega)$ is the ionisation rate over a laser period and $\bar{J}(x,t)$ is the probability current averaged over a laser period. The added factor of 2 in (2.53) comes from the symmetry of the atomic system where the probability current can flow through the surface at both the left and the right of the atom. The current, in turn, is calculated from

$$J(r,t) = \frac{i}{2}\left(\psi\frac{\partial\psi^*}{\partial x} - \frac{\partial\psi}{\partial x}\psi^*\right). \tag{2.54}$$

Thus, given the wave function in (2.54), the ionisation rate can be directly calculated by the TDSE. In the original paper, the laser light is assumed to be linearly polarised and spatially uniform. To demonstrate the solution process of arriving at an ionisation rate from the TDSE, a δ-potential is used, and the Schrödinger equation takes the form

$$\left(i\frac{\partial}{\partial t} + \frac{\partial^2}{\partial x^2} + E(t)x\right)\psi(x,t) = -\kappa\delta(x)\psi(x,t). \tag{2.55}$$

Here, the electric field is assumed to follow $E(t) = \mathcal{E}_0\cos(\omega_0 t)$ and κ gives the strength of the applied δ-potential. By using Green's functions, one can formulate the wave function as an integral equation in the momentum basis, which is then used in (2.54) to arrive at an expression for the current. Then, by Fourier expansion, the expression for the ionisation rate is reached. In order to arrive at the full PPT expression, the δ-potential is dropped for a potential which is assumed to decrease faster than $1/r$ and the equations are changed to 3 dimensions. Further additions to the formula of the original calculations have been determined, see eg Ref. [25–27]. These changes include: using principal quantum numbers, dipole corrections, occupancy numbers, and Stark shifting. Including these changes, the formula used for the PPT-model in the code is:

$$w(E,\omega) = \zeta(E)\left(\frac{3}{2\pi}\right)^{1/2}|C_{n^*,\,l^*}|^2 f(l,m) I_p \left(\frac{2F_0}{E\sqrt{1+\gamma^2}}\right)^{2n^*-|m|-3/2} A_m(\omega,\gamma)\exp\left(-\frac{2F_0}{3E}g(\gamma)\right), \tag{2.56}$$

where it is assumed that the electric field is linearly polarised. The functions in (2.56) are:

$$\zeta(E) = g_m \exp(-2\alpha_{ion} E), \tag{2.57}$$

$$|C_{n^*,\, l^*}|^2 = \frac{2^{2n^*}}{n^* \Gamma(n^* + l^*)\Gamma(n^* - l^* - 1)}, \tag{2.58}$$

$$n^* = \frac{Z}{\sqrt{2I_p^*}}, \tag{2.59}$$

$$l^* = n^* - 1, \tag{2.60}$$

$$I_p^* = I_p + \frac{\Delta\alpha E^2}{2}, \tag{2.61}$$

$$f(l,m) = \frac{(2l+1)(l+|m|)!}{2^{|m|}|m|!(l-|m|)!}, \tag{2.62}$$

$$F_0 = (2I_p^*)^{3/2}, \tag{2.63}$$

$$A_m(\omega,\gamma) = \frac{4}{\sqrt{3\pi}} \frac{1}{|m|!} \frac{\gamma^2}{1+\gamma^2} \sum_{\kappa \geq \nu} e^{-\alpha(\kappa-\nu)} w_m(\sqrt{\beta(\kappa-\nu)}), \tag{2.64}$$

$$w_m(x) = \frac{x^{2|m|+1}}{2} \int_0^1 dt \frac{e^{-x^2 t} t^{|m|}}{\sqrt{1-t}}, \tag{2.65}$$

$$\alpha(\gamma) = 2\left(\sinh^{-1}(\gamma) - \frac{\gamma}{\sqrt{1+\gamma^2}}\right), \tag{2.66}$$

$$\beta(\gamma) = \frac{2\gamma}{\sqrt{1+\gamma^2}}, \tag{2.67}$$

$$g(\gamma) = \frac{3}{2\gamma}\left[\left(1 + \frac{1}{2\gamma^2}\right)\sinh^{-1}(\gamma) - \frac{\sqrt{1+\gamma^2}}{2\gamma}\right], \tag{2.68}$$

$$\nu = \frac{I_p}{\omega} + \frac{|E|^2}{4\omega^3}, \tag{2.69}$$

$$\kappa = \lceil \nu \rceil, \tag{2.70}$$

where g_m is the occupancy number for a state m, α_{ion} is the polarisability of the ion, I_p is the ionisation potential, $\Delta\alpha$ is the difference in polarisability between the ion and the neutral atom, E is the electric field with angular frequency ω and Z is the residue charge of the ion, which is the remaining charge of the atom after ionisation. The main difference between ionisation rates implemented in HarP and the ones implemented in Ref. [25] is the inclusion of the factor $\zeta(E)$ in Eq. (2.56). This factor accounts for the electric dipole that arises due to the separation between the electron and the remaining atom. Thus, this factor is a dipole (DP) correction factor and is also included in a independently developed code called Luna [27], which is used for simulating ultrafast pulse propagation.

Although the ionisation rate in the PPT-model gives fairly accurate results in certain intensity regions, it also comes with certain approximations. Some of these are shared with the Lewenstein model, where SFA and quasi-classical actions are used. These and several other approximations lead to significant overestimation in predicted rates at higher intensities, as well as neglecting irregular effects in the ionisation rates. Thus, in order to compensate for this, tabulated ionisation rates using more advanced methods can also be used in the code. However, depending on the intensity region used of HHG, PPT can also be chosen as the primary ionisation model for the code.

3

Code structure

The details of HarP's structure, which algorithms are used, and which design choices have been made will be presented here. HarP is divided into modules that the user can import in order to simplify development of HarP and the overall structure is independent of one specific module. Specifically, four modules are included in the code: a propagation module, an ionisation module, a MMA module, and a plotting module. Each of these modules relates to one central role HarP aims for, i.e., simulating the whole HHG process. The whole framework is written according to Python's PEP 8 style standard. Each module contains individual methods and objects in order to simplify the user environment as much as possible.

3.1 Propagation module

The propagation module implements the propagation equation (2.7) by using a finite difference scheme called a Crank-Nicolson (CN) scheme [1] [5]. In order to solve the propagation equation, the envelope of the electric field and polarisation density is divided into a series of time slices in order to reduce dimensions. Each time slice of the envelope is propagated independently, neglecting the effects of interactions between slices. This design choice was adopted from the code used for the simulations in Ref. [7] by R. Weissenbilder et al. and is something that is followed in HarP.
This leads naturally to a nested loop structure, where the first loop is iterated over each time slice in the pulse envelope and then for each time slice, the CN scheme is implemented for the full propagation length. In each step of the CN scheme, the following matrix equation is solved for the harmonics

$$AE_q^{m+1} = BE_q^m + F_q^m(E_1^m), \tag{3.1}$$

where A, B are matrices specified in A.3, m is the specific step taken in the propagation direction z, and F_q^m is the source vector for step m. This source vector represents the full source term in Eq. (2.7) and is set to zero for the fundamental field since there is no generation of the fundamental field. The source vector is related to the induced dipole moment d_q and the atomic number density of neutrals $\mathcal{N}_a$ as

$$F_q^m(E_1^m) = \frac{ik_{q0}\Delta z}{\epsilon_0}\left(\mathcal{N}_a^m|d_q(I_1^m)|e^{\arg(d_q(I_1^m))+q\phi(E_1^m)} + \mathcal{N}_a^{m+1}|d_q(I_1^{m+1})|e^{\arg(d_q(I_1^{m+1}))+q\phi(E_1^{m+1})}\right), \tag{3.2}$$

where ϕ is the phase of the fundamental field and I_1^m is the intensity of the fundamental field at step m. Since the dependence of the source vector is only on the fundamental field, the propagation of the harmonic and fundamental fields can be split into two separate loops: a fundamental loop and a harmonic loop. The fundamental loop is run first due to the harmonic loop's dependence on the resulting fundamental field. The overarching structure of both the fundamental and harmonic loops can be seen in the figures below.

[1] For a detailed calculation of the equations used, see A.3

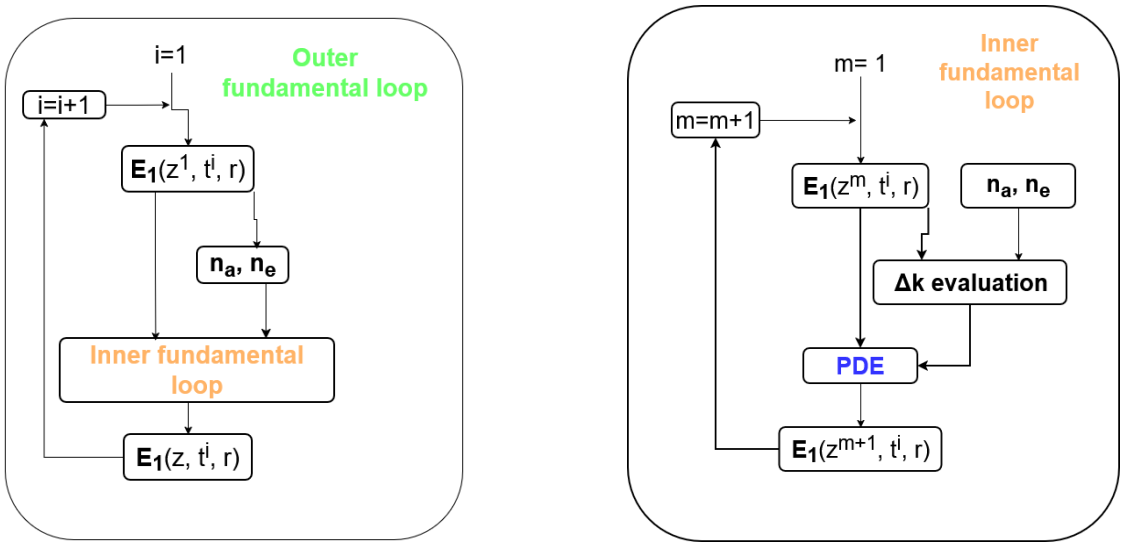

Figure 3.1: Flowcharts showing the structure of both the inner and outer fundamental loop in the propagation module. The outer fundamental loop runs over each time slice of the fundamental field envelope, where each slice is independently run in the inner fundamental loop. For each individual time slice, the inner fundamental loop iteratively solves the partial differential equation (PDE) in Eq. 3.1 for each step in z given $F_q^m(E_1^m) = 0$.

As can be seen in figure 3.1, the phase mismatch Δk_q is calculated in the fundamental loop once every iteration in z and uses the field in the previous step to calculate the Kerr contribution of the phase mismatch.

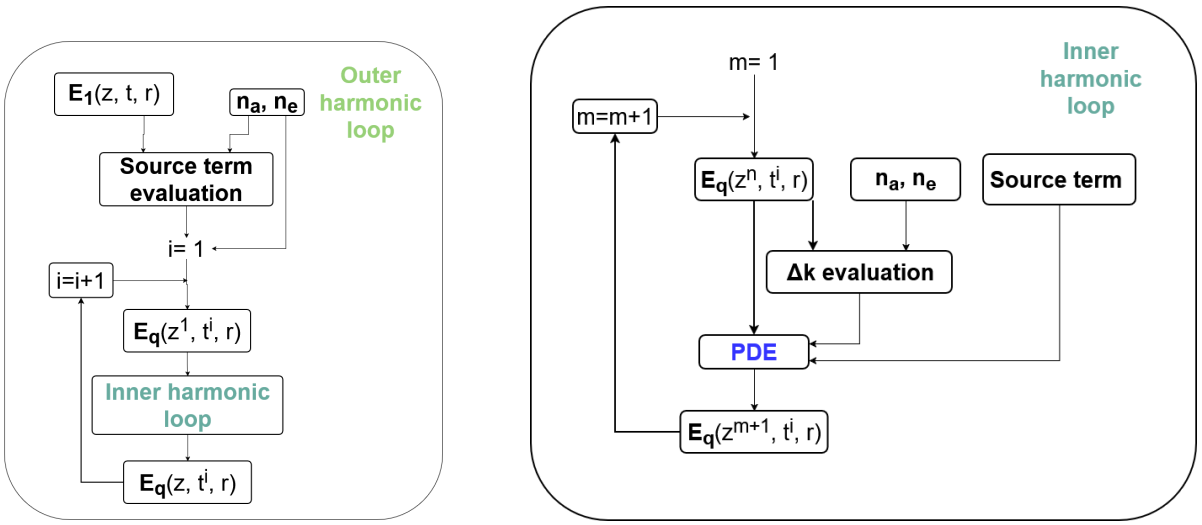

Figure 3.2: Flowcharts showing the structure of both the inner and outer harmonic loop in the propagation module. The propagated fundamental field envelope is used to calculate the source $F_q^m(E_1^m)$ before the harmonic propagation. The outer harmonic loop runs over each time slice of the harmonic field envelope, where each slice is independently run in the inner harmonic loop. For each individual time slice, the inner harmonic loop iteratively solves the partial differential equation (PDE) in Eq. 3.1 for each step in z with the precalculated source.

Inside the fundamental loop, the ionisation of the medium is updated once every new time slice

through the use of methods described in the ionisation module. In general, the ionisation is included by updating the atomic $\mathcal{N}_{\text{at}}$ as well as electronic $\mathcal{N}_e$ densities, affecting all dependent variables further down the loop. Since the highest partial derivative in Eq. (2.3) is two, the discretization of all the terms results in the matrices A and B being tridiagonal (i.e having non-zero values only along the main as well as first sub and super diagonal of the matrix). To efficiently solve the matrix Eq. (3.1), one can use the tridiagonal structure of the matrix, resulting in the use of Scipy's *solve_ banded* method.

Furthermore, the dipole moment in Eq. (3.2) is taken from precalculated tables which contain both amplitudes $|d_q|^2$ as well as arguments $\arg(d_q)$ as a function of intensity and the specific harmonic to be calculated. When an intensity value happens to be in between two tabulated points, a linear interpolation is done in order to get more accurate results. The intensity range for the tables is limited, which then also restricts the operating range, however this does not cause problems here due to the overall large bounds of the tables.

Similarly, the propagation module also uses a tabulated approach in calculating the dynamic polarizability defined in Eq. (2.38). More specifically, the tables are used for specific values of the scattering factors f_1 and f_2 which are procured from NIST's Henke tables [23]. For simplicity, the values of f_1 and f_2 are taken as the nearest neighbouring tabulated value for a given photon energy $E_{\text{photon}} = q\hbar\omega, \forall q \in \mathbb{N}$.

Besides the CN scheme and data processing of the dipole as well as Henke tables, the propagation module also calculates the phase mismatch Δk_q by direct implementation of Eq. (2.31) together with the susceptibilities in Eqs. (2.33) and (2.37).

3.2 Ionisation module

The ionisation module implements two different ionisation models, PPT and TDSE. The PPT-model is calculated according to Eq. (2.56) with the exception of the numerical calculation of the multiphoton sum in $A_m(\omega, \gamma)$, which uses the same numerical handling as described in Ref. [27]. As for the TDSE tables, they are calculated separately by using the Lewenstein integral (2.49) for a specific element and provided as finished tables which are the same the ones as used by Robin Weissenbilder et al in Ref.[7]. Currently, the only implemented element is argon. But given the same data format, other elements can easily be implemented.

The implementation of the PPT-model is done by generating tables for a range of intensities specified by the user. The tables themselves only contain two columns, where the first column is the range of intensities and the second column is the corresponding ionisation rates, calculated by PPT. The PPT-rates themselves are computed using atomic units (a.u) and then converted back to SI, which is done for simplicity. The TDSE tables are generated from direct numerical calculations of TDSE. Schematically, the rates are calculated by keeping track of the overall loss of probability coming from a tunnelling electron's wave function $|\Psi\rangle$ when there is an absorbing potential at the edge of the simulation box as described in Ref. [28].

When the algorithm propagates one step in z, the new ionisation rates are calculated by taking the new intensities on the rt-grid at the new z and finding the corresponding ionisation rates. If the intensity falls between two tabulated intensities, an exponential interpolation is done in order to

find the most suitable approximation of the correct value. The underlying reason for an exponential interpolation is that the rates themselves are almost exponential for PPT, with a small exception for the precalculated rates using the TDSE. The TDSE rates increase almost exponentially to a point where they drop off in a similar fashion. However, since the interpolation is done in such a small interval and the exponential interpolation also can accommodate inverse exponentials, the interpolation stays within reasonable bounds. Given that there is an intensity I_b in between two tabulated intensities $I_1 < I_b < I_2$, the following interpolation is done.

Suppose the true intensity value lies in-between two intensity values I_1 and I_2 where these intensities correspond to some ionisation rate $w(I_1) = w_1$ and $w(I_2) = w_2$. Now, we would like to fit some function $w(I_b)$ given the endpoints and the corresponding intensities at the endpoints. This leads to the general constraint on the function

$$\begin{cases} w(I_1) = w_1, \\ w(I_2) = w_2. \end{cases} \tag{3.3}$$

Since the only known values are w_1 and w_2, the number of unknown coefficients for the interpolation needs to be at maximum two in order to have a determined system of equations. Thus, the general idea used for interpolation is

1. Define the form of the function (e.g., logarithmic, linear, etc.).
2. Use the constraints (3.3) on the defined function.
3. Solve for the unknowns in terms of the constraints and finalise the form.

As mentioned before, the ionisation rate tends to grow in an exponential manner, so it is reasonable to fit a linear function between the two ionisation degree data points in log space (i.e. an exponential fit). Thus, the form of the function is given by

$$\ln(w(I_b)) = aI_b + b, \tag{3.4}$$

where a, b are the unknown coefficients and $w(I_b)$ is the unknown ionisation rate for the intensity value I_b in between the tabulated values. The general form of (3.4) is akin to fitting an exponential function in regular space. Imposing the general conditions results in the solved coefficients

$$\begin{cases} a = \frac{\ln(w_2)-\ln(w_1)}{I_2-I_1} \\ b = \ln(w_1) - \frac{\ln(w_2)-\ln(w_1)}{I_2-I_1} I_1, \end{cases}$$

which, when applied to the general expression in equation (3.4) gives the final interpolation as

$$\ln(w(I)) = \frac{\ln(w_2) - \ln(w_1)}{I_2 - I_1}(I - I_1) + \ln(w_1), \tag{3.5}$$

which is implemented in the code.

Besides the implementation of different ionisation models, the ionisation module also updates the number density according to the solution of (2.27) by direct discretisation and recurrence.

$$\mathcal{N}_a(t + \Delta t) = \mathcal{N}_a(t)e^{-w\Delta t}, \tag{3.6}$$

where $\mathcal{N}_a(t)$ is the number density of neutrals at the current time step t and $\mathcal{N}_a(t + \Delta t)$ is the updated number density at the next step $t + \Delta t$. By unravelling the recurrence relation, we get back the original solution as described in (2.29).

3.3 MMA module

The MMA module is used for benchmarking and compatibility purposes, containing mostly methods for fetching and processing data so it can be used by other parts of HarP. Such data includes, but is not exclusive to: electric field data for comparison, implemented ionisation rates, and grids in r, z, t for consistency when doing comparisons.

3.4 Plotting module

The plotting module is a formalized way of plotting the outputs from HarP through a plotting manager, providing standardized color plots, graphs for conversion efficiency and on-axis distributions. It is initialized as a plotting manager class which has standardized plotting methods for plotting intensity profiles and conversion efficiencies. When doing comparisons, a child class to the plotting manager class could be initialised, which uses similar methods to the parent class.

4
Results

In this section, the results obtained using the HarP framework are presented and compared with established HHG models. The section focuses on numerical stability, pulse propagation, ionisation dynamics, harmonic generation, and conversion efficiencies in argon gas.

4.1 Stability

To test the stability and reliability of HarP, a number of benchmarks and tests are conducted. The benchmarks are done against results provided from the MMA code in Ref. [4]. Although the MMA code uses a different approach with fewer approximations, it can still be used for benchmarking against HarP in order to verify its validity. Thus, several benchmarks are done on results from HarP and compared with the MMA code. The MMA data was provided from simulations done originally Dr. Dominika Maslárová while everything else, including benchmarks was done directly.

4.1.1 Energy conservation

In order to see how the numerical stability of the laser propagation depends on the choice of grid discretisation, energy conservation is tested. As the resolution decreases, there comes a point where the energy conservation breaks abruptly, which points to an appropriate size of the grid discretisation while conserving computational resources. Since the source in equation (2.7) continually introduces extra energy to the system, energy conservation is only tested for the propagation equation (2.11) of the fundamental laser field. However, the CN scheme in both equations is essentially the same, which means the same general conclusions can be drawn. To measure the energy conservation in a standardized way, the relative error between the input energy H_i and the final energy after propagation H_final are used. The relative error is calculated from

$$\epsilon_\mathrm{error} = \frac{|H_\mathrm{i} - H_\mathrm{final}|}{H_\mathrm{i}} = \frac{\Delta H}{H_\mathrm{i}}, \tag{4.1}$$

where ϵ_error is the total relative error. Furthermore, the grid spacing in a certain dimension is normalized by the total dimension length, giving the normed grid spacing ΔD_Norm as

$$\Delta D_\mathrm{Norm} = \frac{\Delta D}{D_\mathrm{tot}}, \tag{4.2}$$

where ΔD is the grid spacing in a dimension $D = \{z, t, r\}$ and D_tot is the full size of the simulated dimension. Since the propagation in HarP is only done on the envelope of the electric field, the wavelength should not affect the following analysis.

In figure 4.1, a pulse of 0.44 mJ was propagated in vacuum, where $\mathcal{N}_a = 0$. Each dimension z, t, r is independently adjusted while keeping the other stepsizes small. In order to investigate the energy

convergence with the inclusion of phase mismatch, a density is included on top of the same conditions as in figure 4.1.

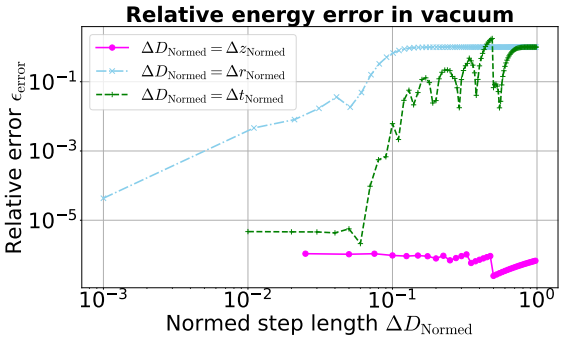

Figure 4.1: The relative error ϵ_{error} as a function of the normed stepsize ΔD_{Norm} for all dimensions, used in vacuum.

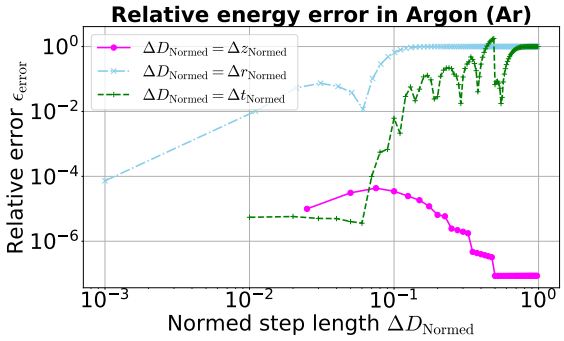

Figure 4.2: The relative error ϵ_{error} as a function of the normed grid spacing ΔD_{Norm} for all dimensions used, in argon with a initial number density of neutrals $n_{a0} \approx 3.941 \cdot 10^{24}$ m^{-3}.

As can be seen in Fig. 4.1, three distinct behaviours are observed when increasing the time step and spatial resolution for each of the dimensions individually. Interestingly, the increase of the time step breaks energy conservation in an oscillating way, whereas an increase in the radial resolution breaks energy conservation constantly after a certain size. Moreover, the error for an increase in grid spacing along the propagation direction in z is almost constantly low over the full range. By comparing the two Figs. 4.1 and 4.2, there seem to be very little difference whether gas is included or not, with the exception of the resolution in the z direction.

In order to show energy conservation during propagation, a simulation is done for a Gaussian pulse in vacuum using the same conditions as those in Fig. 4.1 but with sufficiently small time step and fine spatial resolution in each dimension.

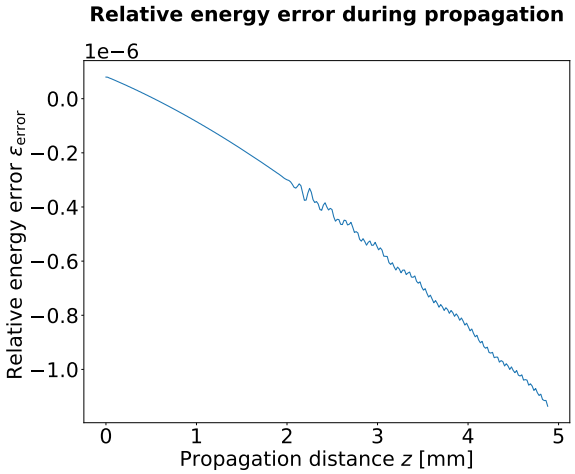

Figure 4.3: The relative energy error ϵ_{error} accumulated during propagation of a Gaussian pulse in vacuum along the propagation axis z.

As can be seen in Fig. 4.3, the accumulated error is of the order 10^{-6} over the full propagation length, showing good numerical stability and energy conservation. Although negligible, there is still a finite violation of energy conservation, which could be due to either numerics or boundary conditions at $r = r_{\max}$ absorbing tiny amounts of energy as the pulse propagates.

4.1.2 Intensity profile comparisons

To test the overall propagation of HarP, on-axis and full intensity distributions are compared with simulations using the MMA approach described in Ref. [4]. The code is run for two specific cases of pressure and length; one at lower pressure with a longer medium (initial gas) length and one at high pressures with a shorter medium length. The effect of pressure is a change in the overall medium density through Eq. (2.26), thus directly affecting the phase mismatch and source terms in the propagation of both fundamental and harmonic fields. More specifically, the choices of pressure and medium length for the two cases are shown in Tab. 4.1 where one case is high pressure, and the other is low pressure.

	Case a)	Case b)
Pressure p (mbar)	148.54	28.98
Length l (mm)	1.56	4.8
Rayleigh length z_r (mm)	18.6	18.6
Pulse energy H_1 (mJ)	0.44	0.44
Pulse duration t_{FWHM} (fs)	22	22
Wavelength λ_1 (nm)	810	810

Table 4.1: Chosen pressures and lengths for two specific simulation cases sharing the same Rayleigh length, pulse energy, pulse duration, and wavelength. Case a) is high pressure with a shorter medium length, while case b) is low pressure with a longer medium length.

The chosen initial pulse has a Gaussian envelope with the parameters shown in Tab. 4.1, propagating in argon for the two cases. Below, the propagation of the two cases can be seen being compared against the MMA approach under similar conditions.

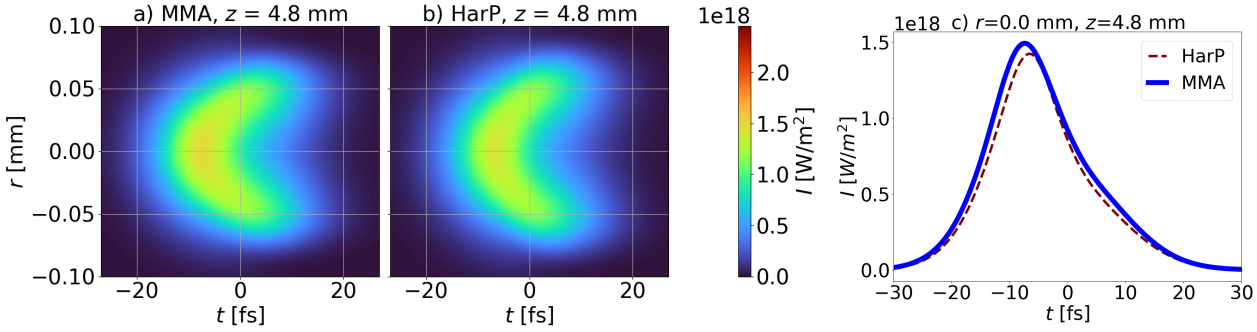

Figure 4.4: a) and b) show the spatial intensity distribution at the end of the medium for case b) in Tab. 4.1. The chosen medium is argon at 28.98 mbar with a Gaussian initial pulse of 22 fs and a medium length of 4.8 mm. a) The MMA approach, which uses its own implemented PPT-model as its ionisation model. b) Harp's intensity profile under the same initial conditions and uses Harp's implementation of PPT without DP-correction as its ionisation model. c) The on-axis intensity distributions ($r = 0$) from a) and b), where HarP and MMA are compared.

From what can be seen in Fig. 4.4 the overall distributions match quite well, with the exception of small differences in the profile. Thus, the overall macroscopic propagation seems to be implemented correctly. Since both approaches differ significantly in how the propagation is performed, the observed differences could possibly be due to differences in approximations between the two approaches.

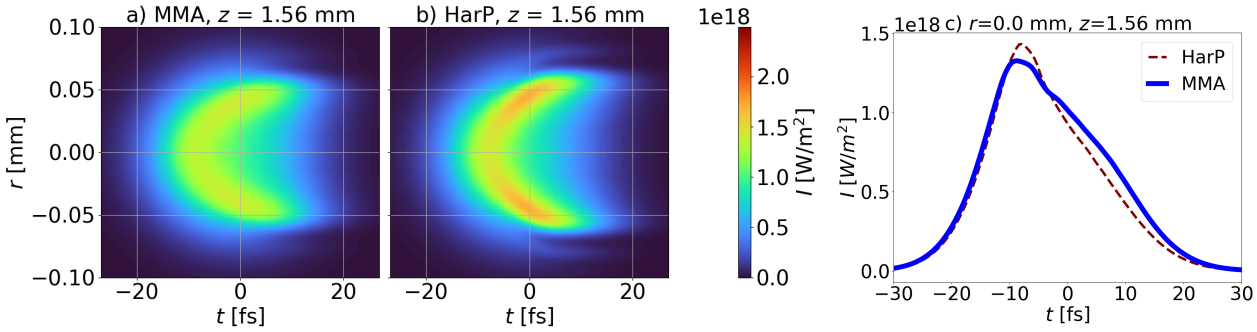

Figure 4.5: a) and b) the spatial intensity distribution at the end of the medium for case a) in Tab. 4.1. The chosen medium is argon at 148.54 mbar with a Gaussian initial pulse of 22 fs and a medium length of 1.56 mm. a) The MMA approach, which uses its implemented PPT-model as its ionisation model. b) Harp's intensity profile under the same initial conditions and uses Harp's implementation of PPT without dipole correction as its ionisation model. c) The on-axis intensity distributions ($r = 0$) from a) and b), where HarP and MMA are compared.

Comparing Figs. 4.4 and 4.5, there seems to be a larger difference for the high pressure case than for the low pressure one. It can also be noted that when looking at the spatial profile in Figs. 4.5 a) and b), the width of the propagated pulse differs slightly. Moreover, on the same figure, the radial intensity profile also seems to be slightly more inhomogeneous for HarP than for MMA, although the on-axis profiles seem to match quite well.

4.2 Ionisation

The ionisation models implemented in HarP are PPT-model and TDSE tables. The latter uses ionisation rates calculated from TDSE, where the implemented PPT-formula includes the dipole (DP) correction $\zeta(E)$ as standard. To illustrate as well as compare ionisation models between HarP and MMA, Fig. 4.6 b) contains HarP's PPT-model both with and without the DP-correction as well as the MMA-rates.

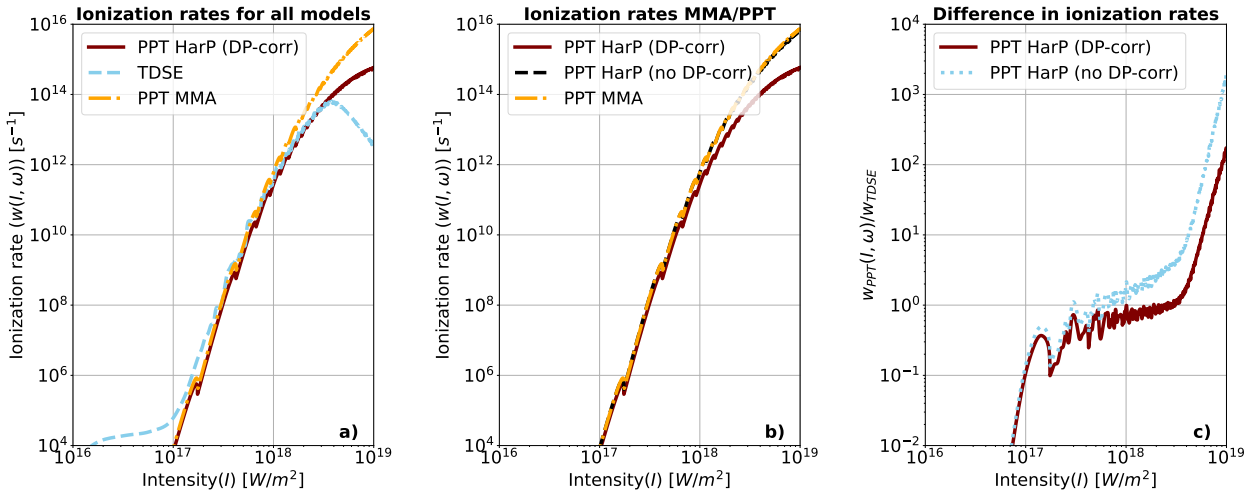

Figure 4.6: Comparisons between the different ionisation models for the two approaches, as well as the quotient between PPT- and TDSE- rates. a) A comparison between the implemented PPT-rates with a DP-correction (maroon), the MMA rates (yellow), and the implemented TDSE rates (light blue) over an intensity range between $10^{16} - 10^{19}$ W/m^2. b) A comparison between the PPT-rate in HarP with dipole correction (maroon), the MMA rate (yellow), and the PPT-rate in HarP without a dipole correction. c) The ratio between PPT and TDSE rates in order to show how well the PPT model compares to the TDSE rates.

As can be seen in Fig. 4.6, the ionisation rates displayed seem to diverge from the TDSE rates and also from each other at higher intensities, resulting in different ionisation by the fundamental field as it propagates, which affects pulse shaping. In order to investigate the effects of ionisation on the fundamental field, simulations of case a) presented in Tab. 4.1, have been performed using the different ionisation models, which are displayed in Fig. 4.7.

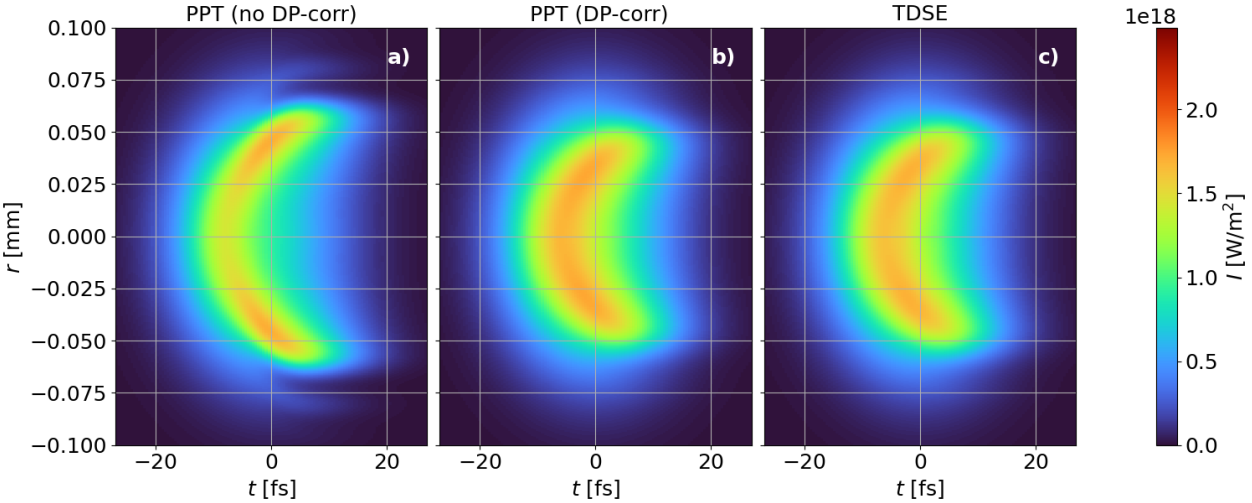

Figure 4.7: Intensity I of the laser pulse at the end of propagation using the HarP code for case a) in Tab. 4.1, using different ionisation models: a) PPT-formula without DP-correction, b) PPT-formula with DP-correction, and c) TDSE tables.

As can be seen, the influence of ionisation affects the pulse shaping strongly, resulting in very

different profiles and distributions. It can also be seen that by using the dipole correction in the PPT-formula, the ionisation results in more similar pulse shaping for the fundamental field as in the case for the TDSE tables. However, since the TDSE rates uses fewer approximations compared with the PPT-models, the rates used forward in Sec. 4.3 will be the TDSE rates when generating harmonics.

4.3 Harmonic generation

In order to check the harmonic generation and conversion efficiencies, harmonic profiles have been obtained for a Gaussian fundamental pulse with the same parameters as those in Tab. 4.1. As well as those in Tab. 4.1, additional pressures and medium lengths were used. The specific choices for pressures and lengths are taken such that they follow the optimum hyperbola for conversion efficiencies in Ref. [7] and described in Sec. 2.1. For the harmonic profiles, the 23rd harmonic has been chosen with argon as the medium, using the cases in Tab. 4.1 as the fundamental pulse.

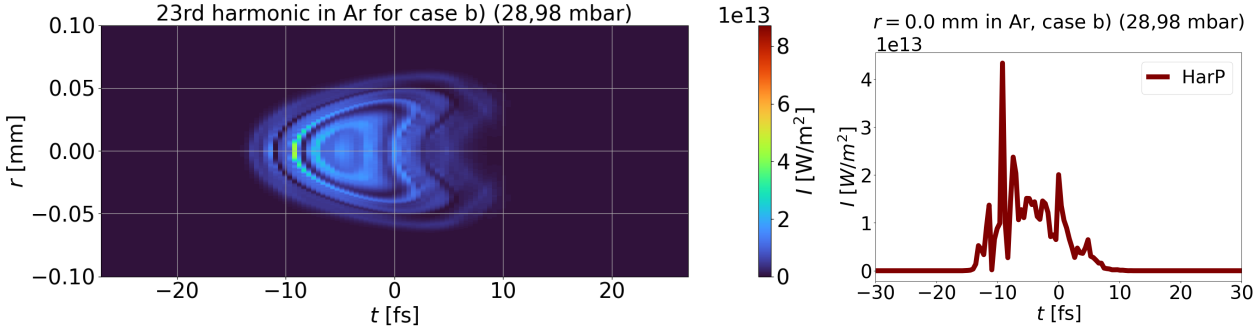

Figure 4.8: Intensity distribution (left) and on-axis intensity distribution (right) for the 23rd harmonic in argon, using the parameters for case b) in Tab. 4.1 as the fundamental pulse.

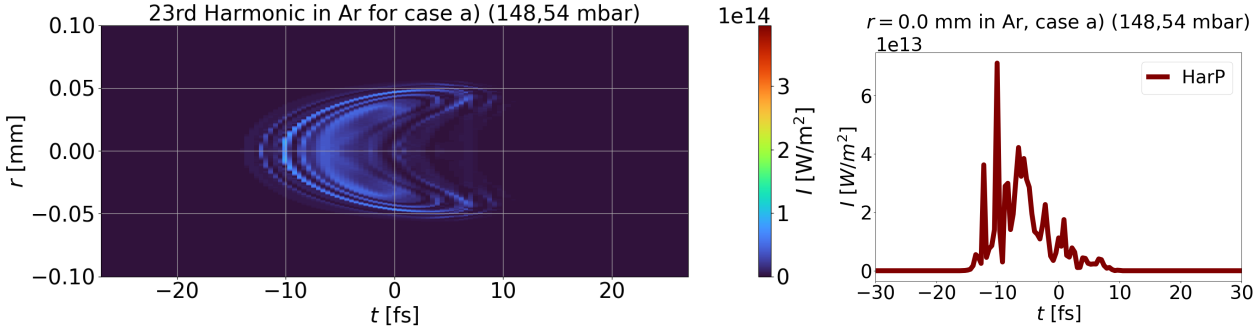

Figure 4.9: Intensity distribution (left) and on-axis intensity distribution (right) for the 23rd harmonic in argon, using the parameters for case a) in Tab. 4.1 as the fundamental pulse.

Since harmonic generation only occurs where the fundamental intensity is present, the overall shape of the generated harmonic should be similar to the fundamental field. Looking at the profiles of the harmonics in Figs. 4.8 and 4.9, the spatial shape of the harmonics is qualitatively similar to the shape of the fundamental pulse, thus indicating that HarP's harmonic generation is working correctly.

4.3.1 Conversion efficiencies

Using the TDSE rates, six simulations were performed using a Gaussian initial pulse for the fundamental field. The simulation parameters were chosen along the optimum pressure-length hyperbola discussed above, including the two cases listed in Tab. 4.1. The conversion efficiency was calculated for each case and the results are shown in Tab. 4.2.

Case	1	2	3	4	5	6
Pressure p (mbar)	148.54	82.48	45.80	28.98	23.82	17.18
Length l (mm)	1.56	2.26	3.29	4.80	6.98	10.16
Rayleigh length z_r (mm)	18.6	18.6	18.6	18.6	18.6	18.6
Pulse energy H_1 (mJ)	0.44	0.44	0.44	0.44	0.44	0.44
Pulse duration t_{FWHM} (fs)	22	22	22	22	22	22
Harmonic q	23	23	23	23	23	23
Conversion efficiency η $\times 10^6$	**4.47**	**3.84**	**2.68**	**2.01**	**1.92**	**1.26**

Table 4.2: Table containing conversion efficiencies at different pressures p and medium lengths l. All the simulation cases use the same initial parameters for the fundamental Gaussian pulse and is of the same harmonic q.

Looking at the conversion efficiencies in Tab. 4.2, they are overall in the same expected range when comparing to the hyperbola described in Ref. [7]. Moreover, the observed decrease in conversion efficiency as the case number increases in Tab. 4.2 aligns with the behaviour of the hyperbola in Ref. [7], further indicating overall correspondence with HarP. However, the acquired conversion efficiencies seem to deviate by approximately a factor of 2 when compared more thoroughly. The source of the discrepancy and whether it can be usefully reconciled remains to be understood.

5
Discussion

In this thesis, the theory of HHG and ionisation has been covered. A nonlinear Helmholtz equation in Eqs. 2.7 and 2.11 has been shown as the main equations, describing the overall generation and propagation of harmonics. Based on this, a numerical framework, HarP, for simulating HHG in gases has been developed and benchmarked. The code combines a CN propagation scheme [5] for solving the macroscopic propagation equations with tabulated microscopic responses obtained from TDSE calculations [6, 7]. A driving laser pulse is propagated through a gaseous medium, where high harmonics are generated through the nonlinear interaction between the laser field and the atoms. The implementation models the generation and propagation of harmonic radiation in gaseous media, including ionisation and phase-matching effects relevant to HHG. To validate the approach, simulations were compared against results from another well-established HHG framework that uses different theoretical and numerical approximations, called MMA [4]. The benchmarks focus on pulse propagation, ionisation dynamics, harmonic spectra, and conversion efficiencies in argon. Overall, the results demonstrate good agreement with established models. They match expected behaviour when it comes to numerical stability, profile comparison with MMA, and ionisation.

When testing numerical stability, HarP follows energy conservation quite well, given sufficiently fine resolution in all respective dimensions. An increasing grid size in both t and r seems to follow the expected patterns when the grid sizes increase. For the relative error in the r direction, the behaviour of an almost linearly increasing relative error until a breaking point is expected. Since the CN scheme has Dirichlet conditions at the radial boundary, which is absorbing energy, a coarser grid in r would also result in a bigger effect of the absorbing region for the field, hence increasing the relative error. Thus, when the grid size in r increases, the absorption directly increases as a result. As for an increasing grid size in t, the relative error is almost constant up to a certain breaking point where the energy error spikes and start to oscillate. The time step determines the number of time slices the envelope is divided into, so it affects both the initial pulse envelope's shape and starting energy. Thus, one possible explanation of the behaviour is that there is a point where the initial envelope is too poorly resolved, resulting in the given energy content before propagation altogether is ill-defined. To further understand possible causes behind the breaking of energy conservation, more simulations are needed that go beyond this work.

In contrast to the step behaviour in t and r, the near-constant error observed when increasing the grid size in z is somewhat unexpected and may arise because the simulated propagation distance in z is too small for the accumulated energy error to change significantly. If this were the case, one should expect little difference in relative error when propagating in a vacuum for a Gaussian pulse, which is what is indeed seen in the simulations. However, when argon is included in the propagation, the relative error seems to first increase, then, after a certain grid size in z, decreases towards zero. Since the only difference between Figs. 4.1 and 4.2 is the inclusion of gas, the new observed behaviour might stem from accumulated errors from both ionisation and dispersion terms.

If these errors accumulate throughout the propagation, there are two opposing effects that influence the total error: the progressive accumulation of errors over many steps, and the magnitude of the error introduced at each step. If the grid size in z is small enough, there are more steps over which errors can accumulate. However, the scale of the errors becomes so small that the total error displayed in Fig. 4.2 also becomes small. On the other hand, if the grid size in z gets large, the size of the error per step becomes larger, at the cost of fewer steps in z over which the error can accumulate. Thus, the expectation of the largest error is when the grid size is large enough so that the error per step is large, and there are still enough steps for the CN scheme to accumulate the error. To better isolate the origin of the observed behaviour, future investigations could compare simulations with controlled numbers of propagation steps in order to distinguish between per-step numerical errors and accumulated propagation errors.

The profile comparison between the MMA and HarP's approach matches very well for the two cases displayed in Figs. 4.4 and 4.5. However, there seem to be small differences in intensity profiles, which also become more pronounced for case a), that is at higher pressure of the medium, in Tab.4.1. One possible reason for the differences in intensity profile between MMA and HarP is partly due to the omission of free currents in the source term for the macroscopic propagation equation, both for harmonics and fundamental fields. If the free currents are dependent on the number density of free electrons, an increase in medium pressure in combination with ionisation could directly affect the size of the free currents. Thus, if the pressure increases while the ionisation degree is the same, the larger the free current becomes, resulting in larger differences between the two approaches. Hence, one thing to investigate further based on the comparison between MMA and HarP would be to consider in more detail the inclusion of free currents and the limiting cases where the exclusion does not hold.

The comparison between implemented ionisation models suggests an overall good agreement between PPT and TDSE rates for a specified intensity region when a DP-correction is included for PPT. However, there are some differences when comparing the PPT in the MMA approach and TDSE rates at higher intensities. When HarP's PPT-model neglects the DP-correction, both HarP's and MMA's PPT-models significantly overlap, suggesting that the main difference in the ionisation models is the DP-correction factor. Simulations of the fundamental field with different ionisation models shown in Fig. 4.7 suggests that pulse shaping of the fundamental field is sensitive to the ionisation rate, which, in combination with the almost exponential nature of the PPT-rates, could result in very different intensity profiles. Looking more closely at Fig. 4.7 a), the fundamental pulse envelope seems to have dispersed more in the radial direction as well as being more inhomogeneous due to the increased ionisation. One interesting continuation of this analysis would be to investigate the impact of higher ionisation on the generated harmonics. Intuitively, the increase of ionisation in the medium could result in a reduction in the density of neutrals in the medium by the update in Eq. (2.27), thereby directly reducing the size of the source in Eq. (2.3). From this, the reduction in source amplitude would reduce harmonic generation and thus also conversion efficiency η.

As pointed out earlier in Sec. 4.3, the overall shape and appearance of the generated harmonics in Fig. 4.8 as well as 4.9, qualitatively match the overall shape of their respective fundamental field. One reason why this should be the case is that the harmonics themselves experience the same ionisation as the fundamental field, resulting in similar shaping of the harmonics. Furthermore, the intensity profiles of the 23rd harmonic in Figs. 4.8 and 4.9 show a striped pattern, which is also visible in their respective on-axis distribution. This pattern could possibly show the phase mismatch

Δk_q of the harmonics as described in Sec. 2.

The simulated conversion efficiencies in Tab. 4.2, as concluded earlier, are in the same overall range while also being roughly a factor of 2 off. Within the theoretical framework in this thesis, the conversion efficiency is dependent on the intensity of the generated harmonic fields. For HarP, the intensity of the harmonic field is determined by the complex interaction between three variables: the phase mismatch Δk_q, the ionisation, and the source term described by Eq. (3.2). Since HarP uses a tabulated approach for the atomic response, the mentioned variables depend fundamentally on the tabulated data. If the dynamic that determines the intensity of the harmonic field is sensitive to small changes of the tabulated values, the difference observed could come down to the specific use of tables. However, the tables used for the source and ionisation was provided by the authors of Ref. [7] and the tables for the scattering factors f_1 and f_2 presented in Eq. (2.38) should be the same as the ones referred to in Ref. [7]. So, given that the tables being used are understood to be the same, the formulas using them could either differ slightly, which, together with a possibly rather sensitive dynamic, could account for the factor of 2 discrepancy. Therefore, a significant amount of future work remains regarding the conversion efficiency, for instance exploring the results of simulating the full hyperbola for a wider set of pressures and lengths in HarP.

5.1 Outlook

While overall the results presented demonstrate a fair degree of success, there exist aspects to investigate further and to improve on for further updates regarding HarP. Even though the profile match between the MMA approach and HarP was successful, there seems to be a small discrepancy in the overall pulse profile. One possibility that might cause such a difference in behaviour might be HarP's exclusion of free currents in the propagation equation. While small, whether the inclusion of free currents might affect the resulting profile in any noticeable way remains to be seen. One other direct improvement of HarP's speed and performance would be to switch from Scipy's *solve_ banded* method to an implementation of the Thomas algorithm to solve the tridiagonal matrix Eq. (3.1). When solving for multiple harmonics for a given fundamental field, the loop structure for the CN scheme is subject to parallelization, providing possible improvements to simulate multiple harmonics at the same time. Moreover, the current architecture of HarP, as described in Sec. 3, could also be further improved by leaning into an even more object-oriented design, which could improve the overall user experience.

Also, since HarP is using a tabulated approach for the microscopic response, further additions could be to implement programs that generate the necessary tables, allowing the exploration of even more parameters, such as dependence on the fundamental wavelength or choice of elements, making HarP more general in its simulation capability.

Several other investigations can be done in order to further explore the theoretical aspects of HarP's approach, for example, by investigating the limitations of HarP's underlying approximations. Based on these results, valid operating ranges can be defined. Since there has only been available data for argon, other elements such as krypton and neon could be investigated if valid tables could be procured. On the same note, other wavelengths of the driving laser could be further investigated in order determine any wavelength dependence in conversion efficiency, ionisation, and overall propagation.

Further benchmarks could be done against theory, such as reconstructing the hyperbola for conversion efficiencies as well as the harmonic spectrum, where the harmonic cut-off in the spectrum could be compared with predictions made from the three-step model. Moreover, benchmarks demonstrating the computational speed when compared with other non-tabulated approaches could be done in order to further show the specific speed advantages of this approach.

5.2 Conclusions

In summary, a code to model high harmonic generation and propagation, HarP, has been developed, and described in this thesis from both a theoretical and computational perspective. Furthermore, simulations were done in order to test energy conservation, pulse propagation, and harmonic generation. The results show overall good agreement with expectations and the available literature, but with some minor difference, which may be understood with further research along the lines indicated in Sec. 5.1. Thus, both HarP and the used approach could serve as a lightweight and sufficiently accurate code for simulating HHG in gases.

Bibliography

[1] T. Maiman. Stimulated optical radiation in ruby. *Nature*, 187:493–494, 1960. doi: https://doi.org/10.1038/187493a0.

[2] M. Ferry, A. L'Huillier, X. F. Li, L. A. Lompre, G. Mainfray, and Manus. C. Multiple-harmonic conversion of 1064 nm radiation in rare gases. *Journal of Physics B: Atomic, Molecular and Optical Physics*, 21:L31–L35, 1988. doi: 10.1088/0953-4075/21/3/001.

[3] A. McPherson, G. Gibson, U. Johann, T. S. Luk, I. A. McIntyre, K. Boyer, and C. K Rhodes. Studies of multiphoton production of vacuum-ultraviolet radiation in the rare gases. *Journal of the Optical Society of America B*, 4(4):595–601, 1987. doi: https://doi.org/10.1364/JOSAB.4.000595.

[4] J. Vábek, T. Němec, S. Skupin, and F. Catoire. Modular multiscale approach to modelling high-harmonic generation in gases. *arXiv*, July 2025. doi: 10.48550/arXiv.2507.04115. URL `https://arxiv.org/abs/2507.04115`.

[5] J. Crank and P. Nicolson. A practical method for numerical evaluation of solutions of partial differential equations of the heat conduction type. *Mathematical Proceedings of the Cambridge Philosophical Society*, 43(1):50–67, 1947. doi: 10.1017/S0305004100023197.S2CID16676040.

[6] A. L'Huillier, P. Balcou, S. Candel, K. J. Schafer, and K. C. Kulander. Calculations of high-order harmonic-generation processes in xenon at 1064 nm. *Physical Review*, 46(5):2778–2790, 1992. doi: https://doi.org/10.1103/PhysRevA.46.277.

[7] R. Weissenbilder, S. Carlström, L. Rego, and et al. How to optimize high-order harmonic generation in gases. *Nat Rev Phys*, **4**:713–722, 2022. doi: https://doi.org/10.1038/s42254-022-00522-7.

[8] Boyd. R. W. *Nonlinear Optics*. Elsevier, 2003.

[9] M. Lewenstein, P. Balcou, M. Y. Ivanov, A. L'Huillier, and P. B. Corkum. Theory of high-harmonic generation by low-frequency laser fields. *Physical Review A*, 49(3):2117–2132, 1994. doi: https://doi.org/10.1103/PhysRevA.49.2117.

[10] R. W. Boyd. Order-of-magnitude estimates of the non linear optical susceptibility. *Journal of Modern Optics*, 49(3):367–378, 1999.

[11] D. Gabor. Theory of communication. *Journal of the Institution of Electrical Engineers-Part III: Radio and Communication*, 93(26):429–457, 1946. doi: https://doi.org/10.1049/ji-3-2.1946.0076.

[12] R. Weissenbilder. *Optimization of high-order harmonic generation for attosecond science*. PhD thesis, Department of Physics, Lund University, 2023.

[13] E. Constant, D. Garzella, P. Breger, E. Mével, Ch. Dorrer, C. Le Blanc, F. Salin, and P. Agostini. Optimizing high harmonic generation in absorbing gases: Model and experiment. *Physical Review Letters*, 82(8):1668, 1999.

[14] D. K. Cheng. *Field and Wave Electromagnetics*. Pearson Education Limited, 2 edition, 2014.

[15] S. Larsson and V. Thomée. *Partial Differential Equations with Numerical Methods*, volume 45 of *Texts in Applied Mathematics*. Springer-verlag, 2003. ISBN 3-540-01772-0.

[16] Z. Wang, Z. Zhang, X. Zhizhan, and L. Qiang. Space–time profiles of an ultrashort pulsed Gaussian beam. *IEEE Journal of Quantum Electronics*, 33(4):566–573, 1997. doi: https://doi.org/10.1109/3.563385.

[17] Jackson. J. D. *Classical Electrodynamics*. Wiley, 3 edition, 1999.

[18] X. F. Li and A. L'Huillier. Multiple-harmonic generation in rare gases at high laser intensity. *Phys. Rev. A*, 39(11):5751–5761, 1989.

[19] P. B. Corkum. Plasma perspective on strong field multiphoton ionization. *Physical Review Letters*, 71:1994–1997, 1993. doi: https://journals.aps.org/prl/pdf/10.1103/PhysRevLett.71.1994.

[20] P. Antoine, A. L'Huillier, M. Lewenstein, P. Salières, and B. Carré. Theory of high-order harmonic generation by an elliptically polarized laser field. *Physical Review A*, 53(3):1725–1745, 1996. doi: https://doi.org/10.1103/PhysRevA.53.1725.

[21] A. M. Perelomov, V. S. Popov, and M. V. Terent'ev. Ionization of atoms in an alternating electric field. *Soviet Physics JETP*, **23**(5):1393–1409, 1966. URL `https://jetp.ras.ru/cgi-bin/dn/e_023_05_0924.pdf`.

[22] A. Perelomov and V. Popov. Ionization of atoms in an alternating electrical field. iii. *Soviet Physics JETP*, 25:336–343, 1967.

[23] B. L. Henke, E. M. Gullikson, and J. C. Davis. X-ray interactions: Photoabsorption, scattering, transmission, and reflection at e = 50-30,000 ev, z = 1-92. *Atomic Data and Nuclear Data Tables*, 54(2):181–342, 1993. ISSN 0092-640X. doi: https://doi.org/10.1006/adnd.1993.1013. URL `https://www.sciencedirect.com/science/article/pii/S0092640X83710132`.

[24] M. Lewenstein, P. Salières, and A. L'Huillier. Phase of the atomic polarization in high-order harmonic generation. *Physical Review A*, 52(6):4747–4754, 1995. doi: https://doi.org/10.1103/PhysRevA.52.4747.

[25] F. A. Ilkov, J. E. Decker, and S. L. Chin. Ionization of atoms in the tunnelling regime with experimental evidence using hg atoms. *Atomic Molecular and Optical Physics*, **25**(2):4005–4020, 1992. doi: https://doi.org/10.1088/0953-4075/25/19/011e.

[26] A. Couairon and A. Mysyrowicz. Ionization of atoms in the tunnelling regime with eperimental evidence using hg atoms. *Physical Reports*, **441**(2-4):47–189, 2007. URL `https://www.teramobile.org/publications/couairon_mysy_filaments.pdf`.

[27] C. Brahms and J. C. Travers. Luna.jl: A flexible nonlinear optical pulse propagator, 2021. doi: https://doi.org/10.5281/zenodo.5513570.

[28] D. E. Manolopoulos. Derivation and reflection properties of a transmission-free absorbing potential. *Journal of Chemical Phyics*, 117(21):9552–9559, 2002.

[29] M. D. Feit and J. D. Fleck. Light propagation in graded-index optical fibers. *Applied Optics*, 17:3990–3998, 1978. doi: https://doi.org/10.1364/AO.17.003990.

[30] M. D. Feit and J. D. Fleck. Beam nonpariaxiality, filament formation, and beam breakup in the self focusing of optical beams. *Journal of the Optical Society of America B*, pages 633–640, 1988. doi: https://doi.org/10.1364/JOSAB.5.000633.

A
Appendix

A.1 Derivation of the Helmholtz equation in HHG

Given (2.18) and (2.25), the general propagation equation in (2.3) can be reformulated as

$$\left(\nabla^2 - \frac{1}{c^2}\frac{\partial^2}{\partial t^2}\right)\boldsymbol{E} - \frac{1}{\epsilon_0 c^2}\frac{\partial^2}{\partial t^2}\boldsymbol{P}^L = \frac{1}{\epsilon_0 c^2}\frac{\partial^2}{\partial t^2}\boldsymbol{P}^{NL} \longleftrightarrow$$
$$\left(\nabla^2 - \frac{1}{c^2}\left(\frac{\partial^2}{\partial t^2} + \frac{\partial^2}{\partial t^2}\chi^{(1)}\right)\right)\boldsymbol{E} = \frac{1}{\epsilon_0 c^2}\frac{\partial^2}{\partial t^2}\boldsymbol{P}^{NL} \longleftrightarrow$$
$$\left(\nabla^2 - \frac{1}{c^2}\left((1 + (\chi_e + \chi_{at}))\frac{\partial^2}{\partial t^2}\right)\right)\boldsymbol{E} = \frac{1}{\epsilon_0 c^2}\frac{\partial^2}{\partial t^2}\boldsymbol{P}^{NL}.$$

Since the electric field inhibits inversion symmetry, even harmonics are not generated [9]. Hence, the electric field can be expanded as a sum of only odd harmonics. This series expansion, combined with the Fourier transform of the electric field and polarization density as

$$\boldsymbol{P}^{NL} = \frac{1}{2}\sum_q \boldsymbol{\mathcal{P}}_q^{NL} e^{-i\omega q t},$$
$$\boldsymbol{E} = \frac{1}{2}\sum_q \boldsymbol{\mathcal{E}}_q e^{-i\omega q t},$$

where the factor of $\frac{1}{2}$ stems from the convention used in Ref. [6], results in the propagation equation becoming

$$\frac{1}{2}\sum_q \left(\nabla^2 + \frac{1}{c^2}\left(n_q^2\omega_q^2\right)\right)\boldsymbol{\mathcal{E}}_q = -\frac{1}{2}\sum_q \frac{\omega_q^2}{\epsilon_0 c^2}\boldsymbol{\mathcal{P}}_q^{NL}. \tag{A.1}$$

Looking at one specific harmonic q, (A.1) simplifies to

$$\left(\nabla^2 + \frac{1}{c^2}\left(n_q^2\omega_q^2\right)\right)\boldsymbol{\mathcal{E}}_q(r,t) = -\frac{\omega_q^2}{\epsilon_0 c^2}\boldsymbol{\mathcal{P}}_q^{NL} \longleftrightarrow$$
$$\left\{k_q = n_q k_{q,0} = n_q\frac{\omega_q}{c}, \nabla^2 = \nabla_\perp^2 + \frac{\partial^2}{\partial z^2}\right\} \longleftrightarrow$$
$$\left(\nabla_\perp^2 + \frac{\partial^2}{\partial z^2} + k_q^2\right)\boldsymbol{\mathcal{E}}_q = -\frac{k_{q,0}^2}{\epsilon_0}\boldsymbol{P}_q^{NL}.$$

In order to enforce the paraxial approximation as well as the slowly varying envelope approximation (SVEA), one can employ the split operator method as described in Refs.[29, 30]. This is done by

defining the operators

$$\hat{P} = -\frac{k_{q,0}^2}{2\epsilon_0}\boldsymbol{P}_q^{NL}, \tag{A.2}$$

$$\hat{Q}^2 = \nabla_\perp^2 + k_q^2 - \hat{P}, \tag{A.3}$$

$$\hat{T}^2 = \frac{\partial^2}{\partial z^2}, \tag{A.4}$$

which leads to the propagation equation being rewritten as

$$\left\{\left(\hat{T} + i\hat{Q}\right)\left(\hat{T} - i\hat{Q}\right) + i\left[\hat{T}, \hat{Q}\right]\right\}\boldsymbol{\mathcal{E}}_q = 0. \tag{A.5}$$

The factorization of the operators $\hat{Q}$ and $\hat{T}$ in equation (A.5), shows the wave equation is composed of forward and backward propagating waves which interact through $i\left[\hat{T}, \hat{Q}\right]\boldsymbol{\mathcal{E}}_q$. In the cases where $i\left[\hat{T}, \hat{Q}\right] \approx 0$ the refractive index and polarization density varies slowly in the propagation direction on the order of the laser wavelength. If this assumption holds, the equation can be decoupled into forward and backward propagating waves. This decoupling leads to

$$\frac{\partial \boldsymbol{\mathcal{E}}_q}{\partial z} = \pm i\hat{Q}\boldsymbol{\mathcal{E}}_q. \tag{A.6}$$

Using only the forward propagating waves in (A.6), *i.e* the $+i\hat{Q}\boldsymbol{\mathcal{E}_q}$ term in (A.6), the paraxial approximation could be done by Taylor expansion, giving

$$\begin{aligned}
&\frac{\partial \boldsymbol{\mathcal{E}}_q}{\partial z} = i\hat{Q}\boldsymbol{\mathcal{E}}_q \longleftrightarrow \\
&\frac{\partial \boldsymbol{\mathcal{E}}_q}{\partial z} = ik_q\sqrt{1 + \frac{\nabla_\perp^2 - \hat{P}_q}{k_q^2}}\boldsymbol{\mathcal{E}}_q \approx ik_q\left(1 + \frac{1}{2}\left(\frac{\nabla_\perp^2 - \hat{P}_q}{k_q^2}\right)\right) \longleftrightarrow \\
&2ik_q\frac{\partial \boldsymbol{\mathcal{E}}_q}{\partial z} = \left(-2k_q^2 - \nabla_\perp^2 + \hat{P}_q\right)\boldsymbol{\mathcal{E}}_q \longleftrightarrow \\
&\left(2ik_q\frac{\partial}{\partial z} + 2k_q^2 + \nabla_\perp^2\right)\boldsymbol{\mathcal{E}}_q = \hat{P}_q\boldsymbol{\mathcal{E}}_q.
\end{aligned}$$

By applying the operator $\hat{P}_q$ as well as using the slowly varying envelope as

$$\begin{aligned}
\boldsymbol{\mathcal{E}}_q &= \tilde{\boldsymbol{E}}e^{ik_q z}, \\
\boldsymbol{P}_q^{NL} &= \bar{\boldsymbol{P}}_q^{NL}e^{ik_{q,0}z},
\end{aligned}$$

the propagation equation takes the form

$$\begin{aligned}
&\left(2ik_q\frac{\partial}{\partial z} + 2k_q^2 + \nabla_\perp^2\right)\left(\tilde{\boldsymbol{E}}e^{ik_q z}\right) = -\frac{k_{q,0}^2}{\epsilon_0}\bar{\boldsymbol{P}}_q^{NL}e^{ik_{q,0}z} \longleftrightarrow \\
&2ik_q\frac{\partial}{\partial z}\left(\tilde{\boldsymbol{E}}e^{ik_q z}\right) + 2k_q^2\left(\tilde{\boldsymbol{E}}e^{ik_q z}\right) + \nabla_\perp^2\left(\tilde{\boldsymbol{E}}e^{ik_q z}\right) \longleftrightarrow \\
&\left\{2ik_q\frac{\partial}{\partial z}\left(\tilde{\boldsymbol{E}}e^{ik_q z}\right) = 2ik_q\tilde{\boldsymbol{E}}\frac{\partial}{\partial z}e^{ik_q z} + 2ik_q e^{ik_q z}\frac{\partial}{\partial z}\tilde{\boldsymbol{E}} = -2k_q^2\tilde{\boldsymbol{E}}e^{ik_q z} + 2ik_q e^{ik_q z}\frac{\partial}{\partial z}\tilde{\boldsymbol{E}}\right\} \longleftrightarrow \\
&-2k_q^2\tilde{\boldsymbol{E}}e^{ik_q z} + 2k_q^2\tilde{\boldsymbol{E}}e^{ik_q z} + e^{ik_q z}\left(2ik_q\frac{\partial}{\partial z} + \nabla_\perp^2\right)\tilde{\boldsymbol{E}} = -\frac{k_{q,0}^2}{\epsilon_0}\bar{\boldsymbol{P}}_q^{NL}e^{ik_{q,0}z}.
\end{aligned}$$

By rearranging the terms we get:

$$\left(2ik_q\frac{\partial}{\partial z}+\nabla_\perp^2\right)\tilde{\boldsymbol{E}}=-\frac{k_{q,0}^2}{\epsilon_0}\bar{\boldsymbol{P}}_q^{NL}e^{-i\Delta kz} \tag{A.7}$$

This is the resulting inhomogeneous paraxial Helmholtz equation, describing the propagation and generation of harmonics. Although this is the equation used by the Crank-Nicolson scheme, there is another form that is directly used without any exponents. This form is derived by taking the expression in (A.7) and then taking the spatial transform as in Ref. [6]. Thus, employing

$$\bar{\boldsymbol{E}}=\tilde{\boldsymbol{E}}e^{i\Delta kz}, \tag{A.8}$$

and cylindrical coordinates, assuming the solution is independent of the angular coordinate, the resulting propagation equation used directly is

$$\left(2ik_{q0}\frac{\partial}{\partial z}+\frac{\partial^2}{\partial r^2}+\frac{1}{r}\frac{\partial}{\partial r}+2k_{q0}\Delta k_q\right)\bar{\boldsymbol{E}}_q=-\frac{k_{q0}^2}{\varepsilon_0}\bar{\boldsymbol{P}}_q^{NL}. \tag{A.9}$$

A.2 Derivation of dynamic polarizability from scattering theory

Given that plasma effects do not appear in the refractive index, the only effect influencing the refractive index is light scattering on atoms. Thus omitting the electronic susceptibility in (2.25), we have

$$n_q=\sqrt{1+\frac{n_a\alpha_q}{\varepsilon_0}}, \tag{A.10}$$

where α_q is the dynamic polarizability for a harmonic q. Since the harmonics are of higher frequency, their refractive index follows from scattering theory. Given Ref. [23], the complex refractive index n_q can be expressed in terms of atomic scattering factors f_1 and f_2 as

$$n_q=1+\frac{n_a r_e\lambda_q^2}{2\pi}(f_1+if_2), \tag{A.11}$$

where r_e is the classical electron radius, λ_q is the wavelength of the harmonic, and n_a is the number density of neutrals [1]. Equating equation (A.10) and equation (A.11) with each other and then solving for the polarizability α_q gives

$$\begin{aligned}
&\sqrt{1+\frac{n_a\alpha_q}{\varepsilon_0}}=1+\frac{n_a r_e\lambda_q^2}{2\pi}(f_1+if_2)\longleftrightarrow\\
&\frac{n_a\alpha_q}{\varepsilon_0}=\frac{n_a r_e\lambda_q^2}{\pi}(f_1+if_2)+\frac{n_a^2 r_e^2\lambda_q^4}{4\pi^2}(f_1+if_2)^2\longleftrightarrow\\
&\alpha_q=\frac{r_e\varepsilon_0\lambda_q^2}{\pi}(f_1+if_2)\left(\frac{n_a r_e\lambda_q^2}{4\pi}(f_1+if_2)+1\right),
\end{aligned}$$

where the final expression for α_q is

$$\alpha_q=\frac{r_e\varepsilon_0\lambda_q^2}{\pi}(f_1+if_2)\left(\frac{n_a r_e\lambda_q^2}{4\pi}(f_1+if_2)+1\right). \tag{A.12}$$

[1] Note that the sign convention is changed from the original reference in order to be consistent herein.

A.3 Derivation of Crank-Nicolson scheme

The equations used by the propagation part of the code are derived by the Crank-Nicolson (CN) method [5]. The CN-method is an implicit finite difference scheme, used to solve partial differential equations (PDEs) numerically. This method has second order convergence, giving similar accuracy to Runge-Kutta methods of second order (RK2) and midpoint methods but not as precise as RK4 methods. Theoretically, the CN-method is a combination of the backwards as well as forwards Euler methods. More specifically, the CN-method could be outlined as the following. Suppose that we have an equation of the form:

$$\frac{\partial}{\partial z} f = F\left(f, x, z, \frac{\partial}{\partial x}, \frac{\partial^2}{\partial x^2}\right), \tag{A.13}$$

with the given discretization:

$$f(l\Delta x, n\Delta z) \to f_l^n,$$
$$F\left(f, x, z, \frac{\partial}{\partial x}, \frac{\partial^2}{\partial x^2}\right) \to F_l^n,$$

then the method states that:

$$\frac{f_l^{n+1} - f_l^n}{\Delta z} = \frac{1}{2}\left(F_l^{n+1} + F_l^n\right). \tag{A.14}$$

Note in this description, equation (A.14) refers only to evolution with respect to the z-coordinate. However, other variables could easily be considered as well by rearranging the terms so that they are of the same form as equation (A.13). Furthermore, the discretization in equation (A.14), can then be rearranged such that an iterative matrix equation emerges. This iterative equation determines the solution to the given PDE.

For the purpose of evolving harmonics in the z-direction, the equation we would like to discretize is:

$$\left(2ik_{q0}\frac{\partial}{\partial z} + \frac{\partial^2}{\partial r^2} + \frac{1}{r}\frac{\partial}{\partial r} + 2k_{q0}\Delta k_q\right)\boldsymbol{E}_q = -\frac{k_{q0}^2}{\varepsilon_0}\boldsymbol{P}_q^{NL} = \boldsymbol{F}_q. \tag{A.15}$$

By rearranging terms, the form becomes the same as (A.13):

$$\frac{\partial}{\partial z}\boldsymbol{E}_q = -\frac{i}{2k_{q0}}\left(\boldsymbol{F}_q - \left(\frac{\partial^2}{\partial r^2} + \frac{1}{r}\frac{\partial}{\partial r} + 2k_{q0}\Delta k_q\right)\boldsymbol{E}_q\right). \tag{A.16}$$

Before the implementation of the CN-methodology in (A.14), one can discretize the separate terms in the expression as:

$$\boldsymbol{F}_q = F_l^n, \tag{A.17}$$
$$\frac{\partial}{\partial z}\boldsymbol{E}_q = \frac{E_l^{n+1} - E_l^n}{\Delta z}, \tag{A.18}$$
$$\frac{\partial}{\partial r}\boldsymbol{E}_q = \frac{E_{l+1}^n - E_{l-1}^n}{2\Delta r}, \tag{A.19}$$
$$\frac{\partial^2}{\partial r^2}\boldsymbol{E}_q = \frac{E_{l+1}^n - 2E_l^n + E_{n-1}^n}{\Delta r^2}, \tag{A.20}$$
$$\Delta k_q = \Delta k_l^n. \tag{A.21}$$

From the discretization of the individual terms, in combination with equation (A.16), we get the CN-discretization:

$$\frac{E_l^{n+1}-E_l^n}{\Delta z}=-\frac{i}{4k_{q0}}\left(F_l^{n+1}-\left(\frac{E_{l+1}^{n+1}-2E_l^{n+1}+E_{l-1}^{n+1}}{\Delta r^2}+\frac{1}{l\Delta r}\frac{E_{l+1}^{n+1}-E_{l-1}^{n+1}}{2\Delta r}+2k_{q0}\Delta k_l^{n+1}E_l^{n+1}\right)+\right.$$
$$\left.F_l^n-\left(\frac{E_{l+1}^n-2E_l^n+E_{n-1}^n}{\Delta r^2}+\frac{1}{l\Delta r}\frac{E_{l+1}^n-E_{l-1}^n}{2\Delta r}+2k_{q0}\Delta k_l^n E_l^n\right)\right).$$

From this, if we consider $\lambda=-\frac{i\Delta z}{4k_{q0}}$, we can rearrange the terms as:

$$E_l^{n+1}+\lambda\left(\frac{E_{l+1}^{n+1}-2E_l^{n+1}+E_{l-1}^{n+1}}{\Delta r^2}+\frac{1}{l\Delta r}\frac{E_{l+1}^{n+1}-E_{l-1}^{n+1}}{2\Delta r}+2k_{q0}\Delta k_l^{n+1}E_l^{n+1}\right)=E_l^n+$$
$$\lambda\left(F_l^n+F_l^{n+1}-\left(\frac{E_{l+1}^n-2E_l^n+E_{n-1}^n}{\Delta r^2}+\frac{1}{l\Delta r}\frac{E_{l+1}^n-E_{l-1}^n}{2\Delta r}+2k_{q0}\Delta k_l^n E_l^n\right)\right)\Longleftrightarrow$$
$$\lambda\left(\frac{1}{\Delta r^2}-\frac{1}{2l\Delta r^2}\right)E_{l-1}^{n+1}+\left(1-\lambda\left(\frac{2}{\Delta r^2}-2k_{q0}\Delta k_l^{n+1}\right)\right)E_l^{n+1}+\lambda\left(\frac{1}{\Delta r^2}+\frac{1}{2l\Delta r^2}\right)E_{l+1}^{n+1}=$$
$$-\lambda\left(\frac{1}{\Delta r^2}-\frac{1}{2l\Delta r^2}\right)E_{l-1}^{n}+\left(1+\lambda\left(\frac{2}{\Delta r^2}-2k_{q0}\Delta k_l^{n+1}\right)\right)E_l^{n}-\lambda\left(\frac{1}{\Delta r^2}+\frac{1}{2l\Delta r^2}\right)E_{l+1}^{n}+$$
$$\lambda\left(F_l^n+F_l^{n+1}\right).$$

From the last equality, we are given a matrix equation of the form:

$$A\boldsymbol{E}^{n+1}=B\boldsymbol{E}^n+\tilde{F}, \tag{A.22}$$

where A, B are tridiagonal matrices and $\tilde{F}$ is the corresponding source in the Helmholtz equations. Expressions of these matrices can either be seen without boundary conditions in the final equality by considering $l-1$ elements to be the sub-diagonal, the l elements as the diagonal, and the $l+1$ elements to be the super-diagonal. Or, the expressions can be seen further down in (A.27)–(A.29).

A.3.1 Boundary conditions

Since the PDE (A.15) is of second order in r and first order in z, it requires three boundary conditions in order to determine the full solution. When solving PDEs, there are in general two types of conditions that a PDE of the second order can take, namely Neumann and Dirichlet conditions. Dirichlet conditions are conditions which specify the value of the PDE-function at some given boundary. Neumann conditions are similar, but specify instead the value of the derivative of the function at some boundary. In physics, such conditions should be physically motivated as they carry information about the system's behaviour. In the context of HHG, our equation of interest requires three boundary conditions, where each of them can either be a Dirichlet or Neumann condition. In the radial direction, we expect the laser intensity to be zero far from the axis, either because the experiment has some wall or due to the natural decay of intensity off the laser's axis. Furthermore, we also expect the beam on the axis to be smooth at $r=0$. Thus, it is reasonable to assume Dirichlet conditions at $r=r_{max}$ as well as Neumann conditions at $r=0$. Regarding the third condition in z, the initial generation of harmonics at $z=0$ should be zero, because there is no propagation of the fundamental pulse in the medium yet. For the fundamental field, the incoming distribution could either be specified directly or taken from MMA at $z=0$. Hence, the final boundary conditions could

be taken as:

$$\boldsymbol{E}_q\big|_{r=r_{max}} = 0, \tag{A.23}$$

$$\frac{\partial}{\partial r}\boldsymbol{E}_q\bigg|_{r=0} = 0, \tag{A.24}$$

$$\boldsymbol{E}_q\big|_{z=0} = 0, \text{ and } \boldsymbol{E}_1\big|_{z=0} = \boldsymbol{E}_{CUPRAD} \text{ or } \boldsymbol{E}_1\big|_{z=0} = \boldsymbol{E}_{Specified}. \tag{A.25}$$

Given these boundary conditions, how do they change the matrix equation in (A.22)? For the Dirichlet condition in (A.23), the last element $E_{r_{max}}$ of the vector $\boldsymbol{E}^n$ is set to zero. Thus, (A.22) becomes:

$$A\begin{bmatrix} E_1^{n+1} \\ E_2^{n+1} \\ E_3^{n+1} \\ \vdots \\ E_{r_{max}}^{n+1} = 0 \end{bmatrix} = B\begin{bmatrix} E_1^{n} \\ E_2^{n} \\ E_3^{n} \\ \vdots \\ E_{r_{max}}^{n} = 0 \end{bmatrix} + \tilde{F}. \tag{A.26}$$

For the Neumann condition, the discretized derivative at $r = 0$ becomes:

$$\frac{\partial \boldsymbol{E}}{\partial r}\bigg|_{r=0} \iff \frac{E_1^j - E_{-1}^j}{2\Delta r} = 0 \text{ for } j = \{n, n+1\} \text{ and } \{2\Delta r \neq 0\} \iff$$
$$E_1^j = E_{-1}^j.$$

From this, the first row in the matrices A and B in (A.22) can be derived as:

$$\mp\lambda\left(\frac{1}{\Delta r^2} - \frac{1}{2l\Delta r^2}\right)E_{-1}^j + \left(1 \pm \lambda\left(\frac{2}{\Delta r^2} - 2k_{q0}\Delta k_l^{n+1}\right)\right)E_0^j \mp \lambda\left(\frac{1}{\Delta r^2} + \frac{1}{2l\Delta r^2}\right)E_1^j =$$
$$\{\text{Neumann: } E_{-1}^j = E_1^j\} = \left(1 \pm \lambda\left(\frac{2}{\Delta r^2} - 2k_{q0}\Delta k_l^{n+1}\right)\right)E_0^j \mp \lambda\left(\frac{2}{\Delta r^2}\right)E_1^j.$$

As stated before, the incoming condition in z is just a custom condition, taking the initial distribution from MMA or just setting it to zero. Hence, the implementation of such an incoming condition is merely to take the same values at the discretized radial points as the chosen distribution at $n = 0$. Lastly, the full matrices A and B can, in combination with the implemented conditions, be written as:

$$A = \begin{bmatrix} 1-\lambda\left(\frac{2}{\Delta r^2} - 2k_{q0}\Delta k_0^{n+1}\right) & \frac{2\lambda}{\Delta r^2} & 0 & \dots & 0 \\ \lambda\left(\frac{1}{\Delta r^2} - \frac{1}{2\Delta r^2}\right) & 1-\lambda\left(\frac{2}{\Delta r^2} - 2k_{q0}\Delta k_1^{n+1}\right) & \lambda\left(\frac{1}{\Delta r^2} + \frac{1}{2\Delta r^2}\right) & 0 & \dots \\ 0 & \lambda\left(\frac{1}{\Delta r^2} - \frac{1}{4\Delta r^2}\right) & 1-\lambda\left(\frac{2}{\Delta r^2} - 2k_{q0}\Delta k_2^{n+1}\right) & \lambda\left(\frac{1}{\Delta r^2} + \frac{1}{4\Delta r^2}\right) & \dots \\ \vdots & \vdots & \ddots & \ddots & \ddots \end{bmatrix}, \tag{A.27}$$

$$B = \begin{bmatrix} 1+\lambda\left(\frac{2}{\Delta r^2} - 2k_{q0}\Delta k_0^{n}\right) & -\frac{2\lambda}{\Delta r^2} & 0 & \dots & 0 \\ -\lambda\left(\frac{1}{\Delta r^2} - \frac{1}{2\Delta r^2}\right) & 1+\lambda\left(\frac{2}{\Delta r^2} - 2k_{q0}\Delta k_1^{n}\right) & -\lambda\left(\frac{1}{\Delta r^2} + \frac{1}{2\Delta r^2}\right) & 0 & \dots \\ 0 & -\lambda\left(\frac{1}{\Delta r^2} - \frac{1}{4\Delta r^2}\right) & 1+\lambda\left(\frac{2}{\Delta r^2} - 2k_{q0}\Delta k_2^{n}\right) & -\lambda\left(\frac{1}{\Delta r^2} + \frac{1}{4\Delta r^2}\right) & \dots \\ \vdots & \vdots & \ddots & \ddots & \ddots \end{bmatrix}, \tag{A.28}$$

$$\tilde{F} = \lambda\left(F_l^n + F_l^{n+1}\right), \tag{A.29}$$

which are the matrices used in the code in order to solve for the macroscopic propagation of harmonics. For the fundamental propagation, the only difference when it comes to (A.27)–(A.29) is that $\tilde{F}$ is set to zero, since the fundamental does not experience any generation.